LUND UNIVERSITY

Diode-laser absorption spectroscopy - applications in medicine and environmental monitoring

Larsson, Jim

2019

Link to publication

Total number of authors:
1

Diode-laser absorption spectroscopy

– applications in medicine and environmental monitoring

JIM LARSSON
DEPARTMENT OF PHYSICS | FACULTY OF ENGINEERING | LUND UNIVERSITY

Diode-laser absorption spectroscopy

- applications in medicine and environmental monitoring

Jim Larsson

LUND
UNIVERSITY

Organization LUND UNIVERSITY	Document name: Doctoral Dissertaion
Division of Combustion Physics Department of Physics P.O Box 118, SE-211 00, Lund, Sweden	Date of issue 2019-09-03
	CODEN: LUTFD2/TFCP-217-SE
Author: Jim Larsson	Sponsoring organization

Title: Diode-laser absorption spectroscopy – applications in medicine and environmental monitoring

Abstract

A major part of this thesis work has been research in a medical project, where, together with industry and clinical partners, the aim was to develop a prototype system for non-invasive monitoring of premature babies based on the optical measurement technique gas in scattering media absorption spectroscopy (GASMAS). Part of the project was to develop a 3D-printed tissue phantom based on chest X-ray images of the thorax of a premature infant. Experiments were conducted on the phantom, where the oxygen and water vapor content in the lungs were evaluated for different light source- and detector positions. Furthermore, delivery of light with a diffusor attached to the surface of the model was compared with internal light delivery through an optical fiber. A pre-clinical study was performed on anesthetized newborn piglets with different inspired oxygen concentrations and induced lung complications using both dermal and internal light illumination. The measurements with internal illumination were performed by delivering the light through an optical fiber with a diffuse end, and the optical fiber positioned in the esophagus of the piglet. The inspired oxygen concentration was stepwise increased and decreased while measuring the oxygen and water vapor content using two diode lasers emitting at a wavelength of 764 nm and 820 nm, respectively. From the absorption at the two wavelengths an oxygen concentration could be evaluated. When investigating the oxygen content during induced lung complications, i.e., pneumothorax and atelectasis, different responses of the absorption and transmission were identified for the two cases. The project was concluded by a clinical study on healthy newborn infants, where the light was delivered through a diffuser placed in the armpit and the detector was positioned on the thorax of the infant. The initial results are promising; it was possible to detect oxygen absorption signals. However, the study also shows that the system needs further improvements in order to deliver strong enough signals for reliable oxygen diagnostics.

In this thesis, work is also presented on atmospheric monitoring of CO_2 using differential absorption Lidar (DIAL) based on a tunable, continuous-wave (CW) diode laser with an emission wavelength at 1573 nm. The diode laser was coupled to a fiber amplifier to achieve output powers about 1.3 W. The backscattered light was range resolved by arranging the laser beam, collection lens and a line array detector in Scheimpflug geometry, where focus is achieved along the laser beam. This technique is known as Scheimpflug Lidar. From the recorded DIAL curves, CO_2 concentrations of around 400 ppm were evaluated. In addition, aerosol releases in the beam path were studied by observing backscattered light from two diode lasers, one emitting in the near-infrared (980 nm) and the other one in the short-wave infrared region (1550 nm).

Key words: TDLAS, GASMAS, biophotonics, Scheimpflug Lidar, periodic shadowing

Classification system and/or index terms (if any)

Supplementary bibliographical information	Language: English

ISSN and key title ISSN 1102-8718	ISBN 978-91-7895-245-8 (Print) 978-91-7895-246-5 (Pdf)

Recipient's notes	Number of pages: 165	Price
	Security classification	

I, the undersigned, being the copyright owner of the abstract of the above-mentioned dissertation, hereby grant to all reference sources permission to publish and disseminate the abstract of the above-mentioned dissertation.

Signature _____   Date 2019-09-03

Diode-laser absorption spectroscopy
- applications in medicine and environmental monitoring

Jim Larsson

LUND
UNIVERSITY

The road and the tale have both been long, would you not say so? The trip has been long and the cost has been high... but no great thing was ever attained easily. A long tale, like a tall Tower, must be built a stone at a time.
— Stephen King, The Dark Tower

Contents

List of publications

  I. **Development of a compact multipass oxygen sensor used for gas diffusion studies in opaque media**
J. Larsson, L. Mei, P. Lundin, J. Bood and S. Svanberg
Applied Optics **54**, 9772-9778 (2015).

  II. **Development of a 3-dimensional tissue lung phantom of a preterm infant for optical measurements of oxygen – Laser-detector position considerations**
J. Larsson, P. Liao, P. Lundin, E. Krite Svanberg, J. Swartling, M. Lewander Xu, J. Bood, S. Andersson-Engels
Journal of Biophotonics **11**, e201700097 (2018).

  III. **Comparison of dermal versus internal light administration in human lungs using the TDLAS-GASMAS technique – Phantom studies**
J. Larsson, D. Leander, M. Lewander Xu, V. Fellman, J. Bood, E. Krite Svanberg
Journal of Biophotonics, e201800350 (2019).

  IV. **Changes in pulmonary oxygen content are detectable with laser absorption spectroscopy: – proof of concept in newborn piglets**
E. Krite Svanberg, J. Larsson, M. Rasmussen, M. Larsson, D. Leander, S. Bergsten, J. Bood, G. Greisen, V. Fellman
(To be submitted)

  V. **Short-wave infrared atmospheric Scheimpflug lidar**
M. Brydegaard, J. Larsson, S. Török, E. Malmqvist, G. Zhao, S. Jansson, M. Andersson, S. Svanberg, S. Åkesson, F. Laurell, J. Bood
EPJ Web Conferences **176**, 01012, (2018)

VI. **Atmospheric CO$_2$ sensing using Scheimpflug lidar based on a 1.57-µm fiber source**
J. Larsson, J. Bood, C. Xu, X. Yang, R. Lindberg, F. Laurell, M. Brydegaard
Optics Express **27**, 17348-17358 (2019).

Related work

1. **Sensitivity enhancement and fringe reduction in tunable diode laser spectroscopy using hemispherical diffusers**
P. Lundin, M. Karlsson, L. Mei, J. Larsson, G. Somesfalean, S. Svanberg
Review of Scientific Instruments **88**, 053111 (2017).

2. **Computer simulation analysis of source-detector position for percutaneously measured O$_2$ - gas signal in a three-dimensional preterm infant lung**
P. Liao, J. Larsson, E. Krite Svanberg, P. Lundin, J. Swartling, M. Lewander Xu, J. Bood, S. Andersson-Engels
Journal of Biophotonics **11**, e201800023 (2018).

3. **1.57 µm fiber source for atmospheric CO2 continuous-wave differential absorption lidar**
X. Yang, R. Lindberg, J. Larsson, J. Bood, M. Brydegaard, F. Laurell
Optics Express **27**, 10304-10310 (2019).

Populärvetenskaplig sammanfattning

Huvuddelen av detta avhandlingsarbete handlar om att använda laserljus för att undersöka gaser, detta genom att använda laserljus med en våglängd som möjliggör att molekylerna i gasen man vill undersöka interagerar med laserljuset genom en process som kallas absorption. Vad som då händer är att molekylerna i gasen absorberar en del av ljuset, vilket leder till att molekylerna blir mer energirika men också att ljuset man sänder igenom gasen tappar i intensitet. Genom att observera denna process vid olika laservåglängder så kan man få en uppfattning om vilka ämnen som befinner sig i gasen och även hur höga ämneskoncentrationerna är.

En av de stora fördelarna med att använda laser för diagnostik är att det finns möjlighet för icke invasiva mätningar, det vill säga att mätningen inte skall påverka det man mäter. Ett exempel kan vara temperaturmätningar i en flamma vilket kan göras med en termometer, men genom att föra in termometern i flamman kommer flammans egenskaper att förändras och det man i själva verket mäter är temperaturen av en flamma som är delvis blockerad av en termometer. Ett annat exempel är mätningarna på för tidigt födda barn. På grund av deras underutvecklade organ är det av yttersta vikt, att diagnoserna sker med metoder som ofarliga. En annan fördel med laserdiagnostik är att man kan komma åt mätobjekt som inte alltid kan undersökas andra metoder samt att det finns möjlighet att samtidigt mäta gaskomposition och temperatur.

Principen att studera absorption av laserljus har här använts framförallt i tre tillämpningar. I den första studeras gaser som är inneslutna i porösa material. Detta kan till exempel vara trämaterial, där man vill studera hur gas transporteras, båda naturligt och under torkning. Det kan även gälla studier av gassammansättningen i matförpackningar, där läckage och fel gasblandning kan betyda att maten får sämre hållbarhet och att matsvinnet ökar.

Den andra tillämpningen är inom medicinområdet, där författaren medverkat i ett projekt vars syfte är att utveckla ett lasersystem för att undersöka luften i lungorna hos för tidigt födda barn. Projektet motiveras av det faktum att för tidigt födda barn ofta föds med underutvecklade lungor och därmed får tillbringa sin första tid under uppsyn och behandling på en intensivvårdsavdelning. Det finns olika komplikationer som kan uppkomma, men gemensamt är att som standardmetod i diagnos använda röntgenstrålning, dvs joniserande strålning, vilket ökar risken att utveckla elakartade tumörer. Med den optiska teknik som utvecklats inom detta avhandlingarbete öppnas möjligheter för att åtminstone delvis ersätta röntgendiagnostik och därmed minska risken för de ovan nämnda biverkningarna.

En av utmaningarna med att mäta gaser som är inneslutna i porösa material med laserljus är att en stor del av ljuset man skickar igenom materialet kommer att spridas och absorberas av materialet, vilket leder till att ljuset som detekteras efter det har passerat igenom materialet oftast har en mycket låg ljusstyrka. Detta kan liknas vid att använda en ficklampa för att lysa igenom sin hand; på grund av spridning av ljuset i vävnaden så försvinner den runda formen av ljuset som vanligtvis observeras från en ficklampa och absorptionen leder till att det är mestadels rött ljus klarar av att tränga igenom vävnaden. En del av arbetet har varit att utveckla och optimera tekniken, bland annat genom att framställa och utföra studier på 3D-printade modeller samt att genomföra en vetenskaplig studie på spädgrisar.

Mänskligheten står inför enorma utmaningar när det gäller rådande och framtida klimatförändringar. Vi står inför ett läge där det inte längre bara handlar om att undvika klimatförändringarna, utan för den mänskliga civilisationen att anpassa sig. En av de drivande faktorerna till den stadiga ökningen de senaste 140 åren av jordens medeltemperatur, är ökande utsläpp av så kallade växthusgaser. En molekyl som ingår i gruppen växthusgaser är koldioxid, vilken är en restprodukt som skapas vid förbränning av fossila bränslen. Den tredje tillämpningen inom detta avhandlingsarbete rör utveckling och tillämpning av en optisk fjärranalysteknik som bygger på att man sänder laserljus genom atmosfären och sedan avbildar laserstrålen genom att detektera ljus som sprids tillbaka genom interaktion med molekylerna i atmosfären. Genom att använda ljus dels med en våglängd som absorberas av koldioxid och dels av en annan våglängd som inte absorberas så kan man genom att jämföra dessa två signaler mäta hur mycket ljus som koldioxiden i atmosfären har absorberat och därmed räkna ut koncentrationen av koldioxid längs laserstrålen.

Vid sidan av absorptionsbaserade tekniker har även en annan teknik använts, nämligen Ramanspridning. Ramanspridning går ut på att man analyserar den

spridningen som uppstår när laserljus träffar molekyler. Förutom mycket stark spridning på samma våglängd som det pålagda laserljuset genereras även svag spridning på andra våglängder. Denna icke-elastiska process kallas Ramanspridning och uppkommer på grund av att molekylerna i gasen vibrerar och roterar på ämnesspecifika frekvenser, vilket bestämmer vilka våglängder som Ramanspridningen kommer att innehålla. Vidare påverkas fördelningen över vibrations- och rotationsfrekvenser i den uppmätta Ramansignalen av temperaturen, varför Ramanspridning även kan användas för termometri.

Den största nackdelen med Ramanspridning är att den är en svag process, vilket kan göra det svårt att särskilja den intressanta signalen från signaler som uppstår från bakgrundsstrålning och brus. För att få ut så tillförlitlig information som möjligt så vill man att den intressanta signalen ska vara så stark som möjlig samtidigt som man försöker få bakgrundsljuset och bruset så svagt som möjligt. Det finns olika tillvägagångssätt att göra detta på. I denna avhandling har ett filter applicerats som kodar det spridande ljuset med ett randmönster. När man sedan avbildar Ramanspridningen med en kamera kan man, på grund av just denna kodning, särskilja Ramanspridningen från den bakgrund som uppstår av ströljus. Vi har undersökt Ramanspridningen från flammor med olika bränsleblandningar för att analysera filtrets funktionalitet.

Abstract

A major part of this thesis work has been research in a medical project, where, together with industry and clinical partners, the aim was to develop a prototype system for non-invasive monitoring of premature babies based on the optical measurement technique gas in scattering media absorption spectroscopy (GASMAS). Part of the project was to develop a 3D-printed tissue phantom based on chest X-ray images of the thorax of a premature infant. Experiments were conducted on the phantom, where the oxygen and water vapor content in the lungs were evaluated for different light source- and detector positions. Furthermore, delivery of light with a diffusor attached to the surface of the model was compared with internal light delivery through an optical fiber. A pre-clinical study was performed on anesthetized newborn piglets with different inspired oxygen concentrations and induced lung complications using both dermal and internal light illumination. The measurements with internal illumination were performed by delivering the light through an optical fiber with a diffuse end, and the optical fiber positioned in the esophagus of the piglet. The inspired oxygen concentration was stepwise increased and decreased while measuring the oxygen and water vapor content using two diode lasers emitting at a wavelength of 764 nm and 820 nm, respectively. From the absorption at the two wavelengths an oxygen concentration could be evaluated. When investigating the oxygen content during induced lung complications, i.e., pneumothorax and atelectasis, different responses of the absorption and transmission were identified for the two cases. The project was concluded by a clinical study on healthy newborn infants, where the light was delivered through a diffuser placed in the armpit and the detector was positioned on the thorax of the infant. The initial results are promising; it was possible to detect oxygen absorption signals. However, the study also shows that the system needs further improvements in order to deliver strong enough signals for reliable oxygen diagnostics.

In this thesis, work is also presented on atmospheric monitoring of CO_2 using

differential absorption Lidar (DIAL) based on a tunable, continuous-wave (CW) diode laser with an emission wavelength at 1573 nm. The diode laser was coupled to a fiber amplifier to achieve output powers about 1.3 W. The backscattered light was range resolved by arranging the laser beam, collection lens and a line array detector in Scheimpflug geometry, where focus is achieved along the laser beam. This technique is known as Scheimpflug Lidar. From the recorded DIAL curves, CO_2 concentrations of around 400 ppm were evaluated. In addition, aerosol releases in the beam path were studied by observing backscattered light from two diode lasers, one emitting in the near-infrared (980 nm) and the other one in the short-wave infrared region (1550 nm).

Chapter 1

Introduction

The atmosphere of the Earth has a composition with nitrogen N_2 ($\sim 78\%$), oxygen O_2 ($\sim 20.9\%$), water H_2O (from ppm levels up to 5 %), argon Ar ($\sim 0.9\%$) and carbon dioxide CO_2 ($\sim 0.04\%$) [1]. In addition the atmosphere contains trace gases, such as noble gases (Ne and Kr), methane (CH_4) and hydrogen (H_2). The Earth's atmosphere is, with current knowledge, unique in the sense that it contains large amounts of free oxygen (O_2) which is created during photosynthesis and can be an indicator for life [2]. During the history of the Earth, when the atmosphere contained mainly CO_2 and N_2, the increase of oxygen in the atmosphere due to photosynthesis from blue-green algae lead to the oxygen catastrophe [3], where many life forms became extinct. However, the ones that resisted adapted and aerobic organisms evolved.

Today, life forms (e.g. homo sapiens/humans) have evolved with advanced respiratory systems where the uptake of oxygen occurs in the lung organ where gas exchange occurs and oxygen is transported by the blood out to cells in the body. The carbon dioxide created in the metabolism, is then transported back to the lungs and eventually exhaled. It is not difficult to imagine that proper function of the respiratory system is crucial for the chance of survival of the individual. In the larger picture, changes in the atmosphere can affect a population as a whole. A big concern for the future of the human civilization is the climate change [4], with the increase of the global average temperature due to the increase of greenhouse gases in the atmosphere [5]. The greenhouse gases are the molecules in the atmosphere that absorb in the infrared part of the electromagnetic spectrum and this overlaps with the outgoing thermal radiation from earth, and includes CO_2, H_2O and CH_4. Since the start of the industrial revolution (about 1760), the concentration

of CO_2 in the atmosphere has increased by 42 % and has now surpassed 400 ppm [5]. The main source of this increase is combustion of fossil fuels. Other products from the combustion process can also increase the air pollution, which can have harmful effects on the respiratory organs.

There are several types of gas detectors; some common ones are semiconductor [6] and catalytic [7] gas detectors. Their operation principle is that a gas interacting with a surface produces a measurable current, and by analyzing this current the gas content and concentration can be obtained. Other common approaches include optical gas sensors, such as detectors utilizing an infrared light source where gas detection is performed by detecting the reduction of the transmitted light from the light source due to absorption from the gas. Alternatively, gas sensing and monitoring can be performed by using various laser techniques [8]. Some of them will be described in this thesis. An advantage with optical gas detectors is that the gas is interacting with light, making it possible to protect the components. In addition it gives the possibility of open-path gas sensing instead of only point measurements. Using a laser gives the benefits of having a bright, monochromatic and coherent light source.

The main purpose of this thesis is to show the continued development and potential of using lasers and different laser techniques for investigating and monitoring gases in medical, atmospheric and combustion applications. The main focus has been to use diode lasers for gas absorption measurements with a technique called tunable diode laser absorption spectroscopy (TDLAS), including its special case gas in scattering media absorption spectroscopy (GASMAS) when the gas is embedded in a porous material. The techniques are described in Chapter 3, and applications are presented under Medical Applications (Chapter 4) and Remote Sensing (Chapter 5). Then in Chapter 6, another technique, based on inelastic scattering, is discussed for energy applications. A brief introduction of the three areas of research are presented below.

Medical Applications: Every year 130 million babies are born worldwide. Four millions of these will die in their first four weeks of life, in which 99 % are in low and middle-income countries, and it is estimated that 28 % of these are due to preterm births [9]. At birth, preterm babies suffer from underdeveloped organs and may be placed at a neonatal intensive care unit for medical support. A common diagnostic tool for lung complications is to perform chest X-ray imaging. However, this is accompanied with an increased risk of developing malignant tumours [10]. In this thesis, an alternative diagnostic method is investigated by implementation of the GASMAS technique. This method has the potential of

non-invasive, continuous monitoring of the gas content in the lungs of preterm babies [11, 12]. The first part of the project was to create a 3D-printed tissue phantom based on X-ray images of the thorax of a preterm infant to be used for evaluating the technique, e.g. detector and light source positions. Secondly, a pre-clinical study was performed on anesthetized piglets, and lastly a clinical study was performed on healthy newborn babies.

Environmental monitoring: The background concentration of CO_2 is currently slightly above 400 ppm [5] and increasing, contributing to the increase of the average global temperature [13] by reabsorbing the outgoing thermal radiation from Earth, i.e., CO_2 is a greenhouse gas. In addition CO_2 is of interest since it is also an indicator for metabolism and combustion. Obtaining range-resolved information about CO_2 in the atmosphere is possible using Differential Absorption Lidar (DIAL). Commonly in Lidar (Light Detection and Ranging), pulsed laser light is emitted and the backscattered light is collected and temporally resolved. Range is hence obtained from the time delay between emission and detection of the light pulse. In DIAL, gas content is obtained by alternating between laser pulses on and off an absorption line of the atmospheric species of interest. By dividing the two signals, instrument parameters and responses due to atmospheric conditions (except absorption by the targeted species) cancel out, and molecular concentration can be obtained. In this work a novel optical remote sensing technique called Scheimpflug Lidar [14, 15] has been applied for DIAL measurements of CO_2 in the atmosphere. In Scheimpflug Lidar ranging is obtained by having the laser beam, collection lens, and detector array placed in Scheimpflug geometry [16].

Energy Applications: Understanding gas formation and chemical reactions involved in combustion processes, such as burning of fossil fuels or biomass, is required to optimize the energy yield and reduce the amount of pollutants that are produced. A powerful technique for investigation of combustion processes is Raman spectroscopy [17], since it allows detection of multiple species simultaneously. However, the Raman scattered light is weak compared to elastically scattered light and resolving the Raman-shifted spectral lines with a spectrometer may suffer from stray light. In this thesis work, a filtering technique called Periodic Shadowing (PS) [18] has been employed, where the light focused onto the slit of a spectrometer is spatially modulated by a Ronchi grating, and through frequency analysis of the recorded data stray light can be suppressed. The capacity PS technique together with Raman spectroscopy was investigated by studying methane-air flames.

Chapter 2

Molecular Spectroscopy

2.1 Energy structures of molecules

The possible energy states of a molecule are determined by the Eigenstates of the molecular Hamiltonian, and its Eigenvalues are the possible energy levels of the molecule [19]. Due to the complexity of solving the Schrödinger equation for many-body systems, the wavefunction of the molecules can be divided into an electronic and a nuclear component. This treatment of the molecular wavefunction is known as the Born-Oppenheimer approximation [20]. The electronic energy obtained from the electronic wavefunction, which is a function of distance from the nucleus, is then used as a potential for solving the nuclear wavefunction (Fig. 2.1). For each possible electronic state a molecule can possess, the nuclear component describes the vibrational, rotational and translational motion of the molecule. In the rest frame of the molecule and neglecting the nuclear spin, the total energy has contributions from its electronic configuration, vibrational and rotational motion, separately (Eq. 2.1).

$$E_{total} = E_{electronic} + E_{vibrational} + E_{rotational} \qquad (2.1)$$

2.1.1 Electronic states

The electronic configuration of molecules is labeled using a notation [21] (Eq. 2.2) that specifies the total spin angular momentum quantum number, S, and the quantum number corresponding to the z-component of the total orbital angular momentum, Λ, of the molecule. Values of $|\Lambda| = 0, 1, 2, 3, 4...$ are written as
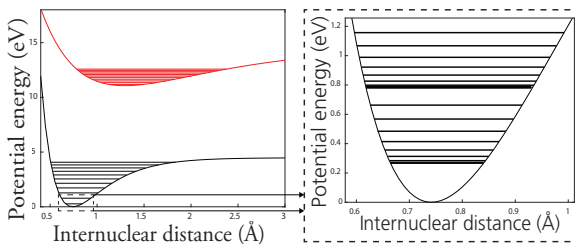
Figure 2.1: Electronic potential of molecular hydrogen H_2 simulated using Morse potentials of the ground state and the first excited state. Zero energy is defined as the minimum of electronic potential of the ground state. The possible energies of the molecule come from the vibrational states that are allowed in each electronic state. The vibrational states exhibit a fine structure due to the rotational motion of the molecule.

$\Sigma, \Pi, \Delta, \Gamma...$, in the same manner as the atomic orbitals (but here with Greek letters instead of Roman). The superscript ($\pm$) denotes if the wave function for Σ states are symmetric ($+$) or anti-symmetric ($-$) in the plane of the molecular axis.

$$^{2S+1}|\Lambda|^{\pm}_{g/u}, \tag{2.2}$$

where $2S + 1$ is the spin multiplicity. The molecular term symbols (Eq. 2.2) are usually accompanied by a letter in front of the symbol, where an X defines the ground state and an uppercase letter, $A, B, C...$, means that the state is a higher excited energy level with the same multiplicity as the ground state. If a lowercase letter is present, $a, b, c...$, it implies higher energy levels with different multiplicity compared to the ground state.

2.1.2   Vibrational states

The energy stored in a molecule due to the relative motion of the nuclei is called vibrational energy, and as a consequence of quantum mechanics, the vibrational energy is quantized. In the case of a diatomic molecule, the electronic potential can roughly be approximated with a Morse potential (Fig. 2.1(a)). In such an anharmonic oscillator the vibrational state is represented by the vibrational quantum number v, which is an integer ($v = 0, 1, 2, 3...$), and the corresponding energy, $E_{vibration}$, given by Eq. 2.3, where ω_e is the fundamental harmonic frequency and $\omega_e x_e$ is the second order vibrational constant which corrects for anharmonicity of the electronical potential. The size of ω_e is on the order of 1000 cm^{-1} to

10^{-1} eV and corresponds to the mid-infrared in the electromagnetic spectrum.

$$E_{vibrational} = (v + \frac{1}{2})\omega_e - (v + \frac{1}{2})^2\omega_e x_e \tag{2.3}$$

The diatomic molecule has only one vibrational mode, which changes the bond length of the molecule, and is thus called a stretching mode. Molecules with more than two nuclei have additional vibrational modes, linear molecules have $3N - 5$ modes and nonlinear molecules have $3N - 6$ vibrational modes, where N is the number of nuclei.

2.1.3   Rotational states

The rotational movement of the molecule around its centre of mass generates an additional energy structure, i.e. rotational energy levels, which also are quantized (Fig. 2.1(b)). In the approximation that the molecule is regarded as an elastic rotor we have for the rotational states, represented with the quantum number J, integer with values ($J = 0, 1, 2, 3...$) the rotational energy, $E_{rotational}$ (Eq. 2.4).

$$E_{rotational} = BJ(J + 1) - DJ^2(J + 1)^2 \tag{2.4}$$

2.2   Light-matter interaction

A change of energy in a molecule, i.e. a transition between two energy states can be possible through interacting with an external electromagnetic field (Fig. 2.2). The molecule can make a transition from a lower to a higher energy state through *absorption* of a photon from the electromagnetic radiation field. The molecule can also interact with a photon from the electromagnetic field in order to make a transition from a higher to a lower energy state. As a result, an additional photon will be created with identical energy and which is coherent with the interacting photon. This process is called *induced* or *stimulated emission*. In addition, a transition from a higher to a lower energy state is also possible through *spontaneous emission* by emitting a photon with an energy corresponding to the energy difference between the two energy states. The rate constants for the three processes are called the Einstein coefficients [22].

In a transition between two states involving electromagnetic radiation, the energy of the photon either emitted or absorbed has to correspond to the difference in energy between the states involved in the transition. For example, in a two-level system with states $|1\rangle$ and $|2\rangle$, and $E_{|2\rangle} > E_{|1\rangle}$, the photon energy needed to

make a transition from $|1\rangle \rightarrow |2\rangle$ is then $E_{photon} = E_{|2\rangle} - E_{|1\rangle}$, and the photon energy is given by

$$E_{photon} = h\nu \qquad (2.5)$$

where h is the Planck constant, and ν is the frequency of the electromagnetic radiation. Depending on the context, the photon energy can either be given in electron volt [eV] or frequency [Hz]. In optical spectroscopy it is common to instead characterize the photon using wavelength, $\lambda = c/\nu$, or wavenumber, $\tilde{v} = 1/\lambda$ which will also be used throughout this thesis.
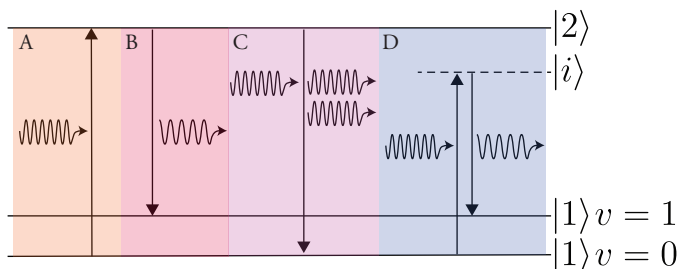
Figure 2.2: Diagram showing the three processes, (A) absorption, (B) spontaneous emission, and (C) stimulated emission, in which a light quantum, photon, can interact with a quantum system such as an atom or molecule. Higher order interactions, involving more than one photon are possible. For inelastic scattering (D) (also known as Raman scattering), the incoming photon is exciting the system to a virtual state, $|i\rangle$, and then de-excited to a state with a different energy as the initial state. The resulting photon has an energy corresponding to the initial photon minus the difference between the two real states involved.

2.2.1   Absorption and the Beer-Lambert law

Light that is propagating through an absorbing medium will have part of its power or intensity absorbed. In 1760, the Swiss scientist Johann Heinrich Lambert published [23] a law of light absorption that stated that the fraction of absorbed light intensity when it passes through a medium with infinitesimal thickness is proportional to the thickness. Later, in 1852, it was discovered by the German scientist August Beer [24] that the fraction of absorbed light intensity is also proportional to an infinitesimal increase in concentration of absorbers.

The two laws are combined into what is known as the Beer-Lambert law and states that light, with a frequency ν and an initial Intensity $I(\nu)$, travelling through

an absorbing medium with length L obtains a reduced intensity, $I'(\nu)$ according to:

$$I'(\nu) = I(\nu)e^{-\alpha(\nu)L} = I(\nu)e^{-N\sigma_a(\nu)L} \qquad (2.6)$$

where $\alpha(\nu)(= N\sigma_a(\nu))$ is the absorption coefficient and $\sigma_a(\nu)$ is the absorption cross-section. It should be noted that the Beer-Lambert law (Eq. 2.6) is valid for an absorbing medium with a homogeneous distribution of absorbers and that the absorbing particles act independently of each other.

The absorption cross section, $\sigma_a(\nu)$, is a measure of the probability that a molecule will make a transition from a lower to a higher energy state by absorbing a photon with frequency ν. The absorption cross section is only non-zero for allowed transitions, i.e. when the energy of the photon corresponds to the energy difference between two energy states of the molecule and if the transition fulfills the quantum mechanical selection rules [19].

For many molecules absorbing from the visible to the microwave part of the electromagnetic spectrum, the *high-resolution transmission molecular absorption database* (HITRAN) [25], provides extensive information about transition frequencies, absorption cross sections and quantum numbers for the energy states. In addition, HITRAN also provides parameters to simulate spectral line broadening., i.e. the lineshape function of $\sigma_a(\nu)$.
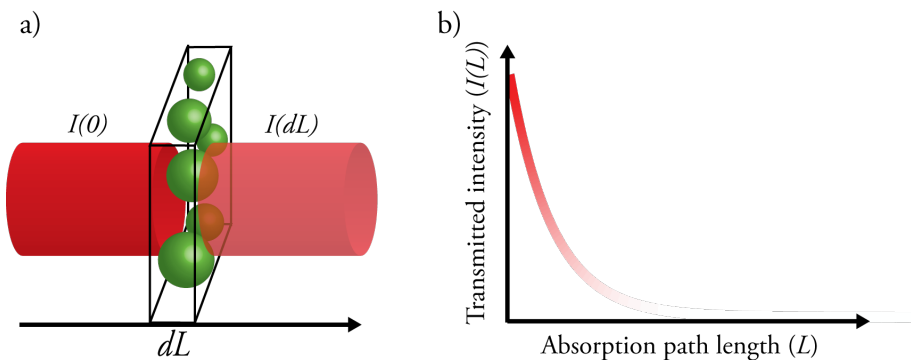
Figure 2.3: (a) For light with a beam cross section area A propagating through an absorbing volume with infinitesimal thickness dL and containing N concentration of absorbing particles with a certain absorption cross-section $\sigma_a(\nu)$, will have some of its intensity absorbed by the medium according to $dI = -I(\nu) \cdot AdL \cdot N\sigma_a(\nu)/A$. (b) Solving the differential equation, $dI/dL = -I(\nu)N\sigma_a(\nu)$ yields the exponential decaying relation known as Beer-Lambert law, $I(L) = I(0)exp(-N\sigma_a(\nu)L)$.

2.3   Line broadening

In spectroscopic measurements, there is always a finite linewidth associated with each spectral line from a transition between two states in an atom or molecule. The lineshape of the spectral line arises due to several mechanisms that contribute to the total lineshape described by the lineshape function $g(\nu)$. In addition, a normalization criterion is applied to the lineshape function. In this section, natural, Doppler and collisional broadening will be briefly discussed.

2.3.1   Natural broadening

For a transition between two states, $|i\rangle$ and $|k\rangle$, with energies E_i and E_k, the interaction with an electromagnetic field is associated with a definite frequency, i.e., $E_i - E_k = h\nu = \hbar\omega$ where $\hbar = h/2\pi$ and $\omega = 2\pi\nu$. However, there is always an uncertainty related to the measurement of energy that is independent of the observer. This is related to Heisenberg uncertainty principle which states that it is not possible to simultaneously determine both the position and the momentum of a particle with unlimited precision.

   The lineshape function due to natural broadening can be derived through various means. In a classical treatment, the electrical dipole can be approximated as a damped harmonic oscillator [26], or it can be obtained through the Einstein coefficients and the uncertainty principle. The shape of the broadening will be Lorentzian with a full width at half maximum, Γ_N, related to the mean life time of the energy level i, τ_i which is the reciprocal of the Einstein coefficient for spontaneous emission, A_{ik}, (Equation 2.7).

$$\Gamma_N = \frac{1}{2\pi\tau_i} = \frac{A_{ik}}{2\pi} \tag{2.7}$$

2.3.2   Doppler broadening

For a molecule traveling with a relative velocity compared to a frame of reference, the frequency, ω_0, of an electromagnetic wave emitted from the molecule will be shifted $\omega = \omega_0 + \vec{k}\cdot\vec{v}$ for an observer placed in the reference frame. Similar for an electromagnetic wave, with a frequency of ω_{abs}, will in the moving frame of the molecule have the possibility to be absorbed if $\omega_0 = \omega_{abs} - \vec{k}\cdot\vec{v}$ or $\omega_{abs} = \omega_0 + \vec{k}\cdot\vec{v}$. Assume that we have particles moving in the z-direction of the reference frame, i.e. $\omega_{abs} = \omega_0 + k_z v_z$, and that they are in thermal equilibrium. The fraction number density of particles in the absorbing state $|i\rangle$, n_i, absorbing frequencies

ω_{abs} are given by the Maxwell-Boltzmann distribution:

$$n_i(\omega_{abs}) = \frac{1}{\Gamma_D\sqrt{\pi}}e^{-(\frac{\omega_{abs}-\omega_0}{\Gamma_D})^2} \tag{2.8}$$

Equation 2.8 is a Gaussian with full-width at half maximum , Γ_D, given by:

$$\Gamma_D = \frac{\omega_0}{c}\sqrt{\frac{2k_bTln2}{m}} \tag{2.9}$$

2.3.3 Collisional broadening

So far we have treated the spectral line broadening due to the natural and the thermal broadening (Doppler broadening). A third mechanism, which in many cases is the dominating contribution to the line shape, is due to collisions between the atom or molecule with the neighbouring gas and therefore goes under the name collisional or pressure broadening. The collisions with the surrounding particles will introduce perturbations to the energy levels and the resulting line broadening will be described by a Lorentzian. The nature of the broadening is sometimes divided into the limiting cases of *impact phase-shift* (weak collisions) and the *static broadening* (strong collisions) [27, 28].

In the *impact phase-shift theory* the collision duration is assumed to be short compared to the time scale for an atom to emit or absorb a photon. If we think of the atom as a radiating dipole, this collision will introduce a change of the phase of the emitted wave and lead to a broadening in the frequency domain. In the case of the *static broadening theory* the collision is instead assumed to be much longer than the radiation time. From the reference system of the atom the perturbing colliders can be viewed as stationary, creating an external electrical field which then affects the radiating dipole. These collisions account for the wings of the line shape profile when collisional broadening is present. However, while the more classical approach gives correct line shapes. Extensive efforts have been carried out to model the collisional broadening using quantum mechanical treatments, both semi-classical using *classical path approximations*, i.e. the colliding particles move in known paths [29]. However, as the above mentioned theories fail to accurately describe the observations, more general quantum mechanical treatments have been developed [30].

For several decades, extensive work has been done in order to characterize collisional broadening parameters. Even though the theory is well-developed, the sheer complexity of calculating the interacting potentials for different atomic and

molecular species means that both theoretical and experimental data are used [31-33]. Parameters such as self- (γ_{self}) and air-broadening (γ_{air}) coefficients and the pressure shift (δ_{shift}) have been compiled for several molecules in the HITRAN database [25], which can then be used to calculate the line width, Γ_L, and line center, $v_0 + \delta_{shift}p$, due to the collisional broadening expressed as the line shape function, ϕ_L:

$$\phi_L = \frac{\Gamma_L/\pi}{(v - v_0 + \delta_{shift}p)^2 + \Gamma_L^2} \tag{2.10a}$$

$$\Gamma_L = (\frac{T_{ref}}{T})^n(\gamma_{air}(p - p_s) + \gamma_{self}p_s) \tag{2.10b}$$

Here the mixing ratio of the self- and air-broadening is determined by the total pressure, p, and the partial pressure, p_s. The broadening coefficients are usually given for certain temperatures, T_{ref}, and need to be scaled, n, for the temperature, T, of interest.

Chapter 3

Tunable Diode Laser Absorption Spectroscopy

The main technique used in this thesis is called *tunable diode laser absorption spectroscopy* (TDLAS) which achieves high spectral resolution by employing a tunable single-mode diode laser and detecting the transmitted light. This resolution allows, e.g., studies of rovibrational lines whose linewidths typically are on the order of GHz (0.01 cm^{-1}). The TDLAS technique dates back to not long after the first semiconductor laser was demonstrated in 1962 [34], when Hinkley et al. [35] performed high-resolution absorption spectroscopy of the transitions at 10.6 µm in SF_6 (sulfur hexafluoride) using a tunable semiconductor laser ($Pb_{0.88}Sn_{0.12}Te$).

In TDLAS (Fig.3.1) a diode laser operating in a single longitudinal mode is scanned in wavelength by adjusting the current through the semiconductor material. High resolution is achieved by the narrowband emission of the diode laser with linewidths achievable down to the kHz region. The emitted light from the laser is transmitted through a volume of gas and then collected on a detector. Since the wavelength is scanned in time by adjusting the injection current, a photo diode or photomultiplier tube (PMT) can be used to detect the transmission as a function of time. In order to obtain an accurate wavelength scale, part of the beam can be passed through a Fabry-Pérot interferometer which will give a relative wavelength scale.
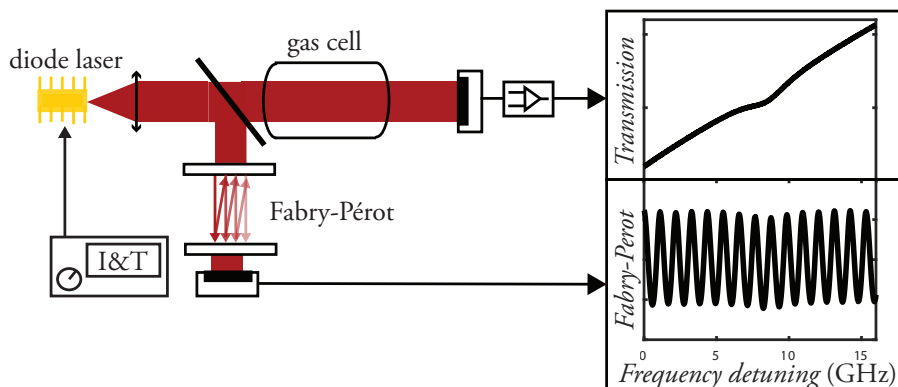
Figure 3.1: Schematic drawing of a typcial TDLAS setup. A diode laser is controlled though the injection current (I) and temperature (T). The emission is collimated and sent through a gas cell with the absorbing species under study. The transmitted light is then collected on a photodiode. Wavelength information is obtained by using a Fabry-Pérot interferometer. In the figure, interference peaks from a low finesse Fabry-Pérot are shown.

3.1 Equipment

3.1.1 Semiconductor laser diodes

The widespread usage of the TDLAS technique in both research and industry [36] can be attributed to the properties of the semiconductor laser diode. They enable robust, compact systems, where the possibility of manufacturing laser diodes with single-mode operation and a wide range of emission wavelengths is utlized.

The main principle behind the laser diode [37] is that the semiconductor material works both as an optical amplifier and a cavity. Population inversion in the semiconductor is achieved by current injection into a heavily doped p-n junction in which the higher energy state, i.e. the conduction band, will be filled (by electrons) and the lower energy state, i.e. valence band, is empty (holes). The cleaved surfaces of the semiconductor will work as partially reflective mirrors. A minimum current is needed in order to obtain optical gain and it is usually specified as the threshold current. The diode lasers used in Papers I-V have a threshold current in the range of 10-30 mA.

The type of diode lasers used in this PhD project is of the distributed feedback (DFB) type, which enables the achievement of single frequency operation. In a DFB laser, a diffraction grating is etched into the material next to the active

region in the semiconductor, which selectively reflects light and allows only a single longitudinal mode to propagate in the semiconductor. Typical output powers lie in the range of 1-100 mW, and wavelength tuning of up to 1-2 nm are possible by adjusting the temperature and current of the laser diode. Output powers up to several Watts are possible by coupling it into an external amplifier. A fiber amplifier was used in Paper VI to obtain single frequency emission around 1573 nm with a 3 MHz linewidth and an output power around 1 W. In that case a DFB laser diode is coupled to an Er/Yb (Erbium/Ytterium) doped fiber which work as the optical amplifier. A multimode diode laser at 975 nm was used as a pump source for the amplifier.

3.1.2   Detectors

The main type of detector used in the absorption measurements performed in the course of this thesis is based on semiconductors. In the work presented in Papers I-IV, a silicon (Si) detector has been used since it has high responsivity between 700-900 nm. The bandgap of Si at room temperature is around 1.1 eV, which translates to a wavelength of roughly 1100 nm. For detecting longer wavelengths, semiconductor materials with a lower energy bandgap have to be used. For example, when performing the DIAL measurements an Indium Gallium Arsenide (InGaAs) array sensor was used to detect the backscattered light at 1573 nm (Paper VI).

3.2   Wavelength Modulation Spectroscopy (WMS)

Absorption spectroscopy is about differentiating between two large signals, the off resonance and the corresponding signal when the laser wavelength is on resonance of a molecular transition. The signal difference to be evaluated is frequently small compared to the recorded total signal, so it can be advantageous to apply some kind of modulation to the signal. In TDLAS, *wavelength modulation spectroscopy* (WMS) is a commonly applied technique in order to enhance the absorption signal [38].

In WMS, the wavelength of the light is sinusoidally modulated at a frequency, f_{mod}, usually on the order of kHz, and at a modulation amplitude, ν_a, which is on the order of GHz (corresponding to the width of the absorption profiles). The emission frequency of the modulated light can then be described as $\nu(t) = \nu_c + \nu_a \cos(2\pi f_{mod} t)$, and when the modulated light interacts with an absorption line there will be a non-linear response in the transmission.

This can be understood by letting ν_c be positioned so that it is off resonance, on the slope or over the peak of the absorption lineshape (Fig. 3.2a). If the modulated signal is completely off resonance it will not experience any absorption and the detected signal is constant, but when ν_c is positioned so that ν_a covers the slope of the absorption profile then the detected signal will obtain an modulation that is repeated at a frequency f_{mod} (Fig. 3.2b). However, when the wavelength modulation overlap with the absorption peak, each modulation cycle will scan over the peak twice and result in two transmission minima in the, time-resolved, detected signal. Demodulating the detected signal either in the time domain using lock-in amplification or in the frequency domain using Fourier analysis will show that the signal contains frequency components that are the modulation frequency f_{mod} and higher harmonics (Fig. 3.2c).
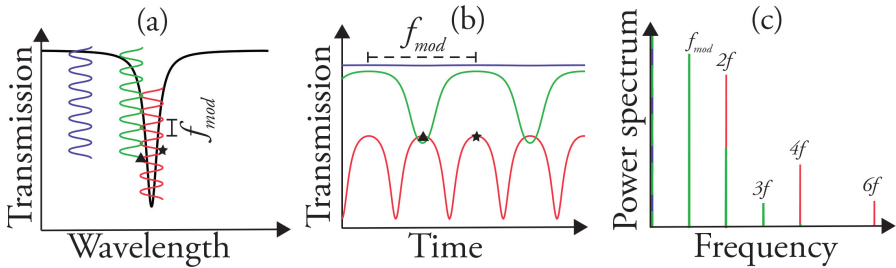
Figure 3.2: Illustration of the signal generation when performing WMS. (a) The wavelength of the light from a laser is modulated at a frequency of f_{mod}, with modulation amplitude, ν_a, (distance from $\triangle$ to $\star$) which is roughly on the same order as the absorption lineshape (black line). The wavelength is fixed with a centre wavelength off resonance (blue), on the slope (green) and on the peak of the absorption profile (red). The time-resolved transmission signal (b) shows no absorption if the wavelength is off resonance (blue) and if on the slope (green) of the absorption profile, the transmission signal will be periodically modulated with f_{mod}. If ν_a overlaps with the absorption peak (red) then two transmission minima are shown in every modulation cycle, f_{mod}^{-1}. In the frequency domain (c) higher harmonics have now been generated.

3.2.1 Lock-in detection using Fourier analysis

In this thesis work, the 2nd harmonic of the wavelength modulated signals, i.e., the 2f signals, were obtained using Fourier analysis of the measured raw signals. The signal (Fig. 3.3a) is Fourier transformed using the fast Fourier transform (FFT) and a frequency scale is constructed by knowing the sampling frequency, f_{sample}

(Fig. 3.3b). Then a bandpass filter, e.g. super-Gaussian filter, is filtering out everything except the information at the 2nd harmonic of the modulation frequency, f_{mod}, and the remaining signal is shifted to zero frequency (step (2) in Fig. 3.3b). Taking the inverse Fourier transform (iFFT) results in a signal containing both a real and an imaginary part (Fig. 3.3c). The signal can be maximized by first finding the phase, φ, between the real and imaginary part at the maximum amplitude. Then the phase is shifted to zero and this is done by multiplying the complex signal with $\exp(-i\varphi)$. The obtained signal, i.e. the real part, is intensity normalized resulting in a 2nd harmonic signal, the amplitude of which is proportional to the absorption (Fig. 3.3d).
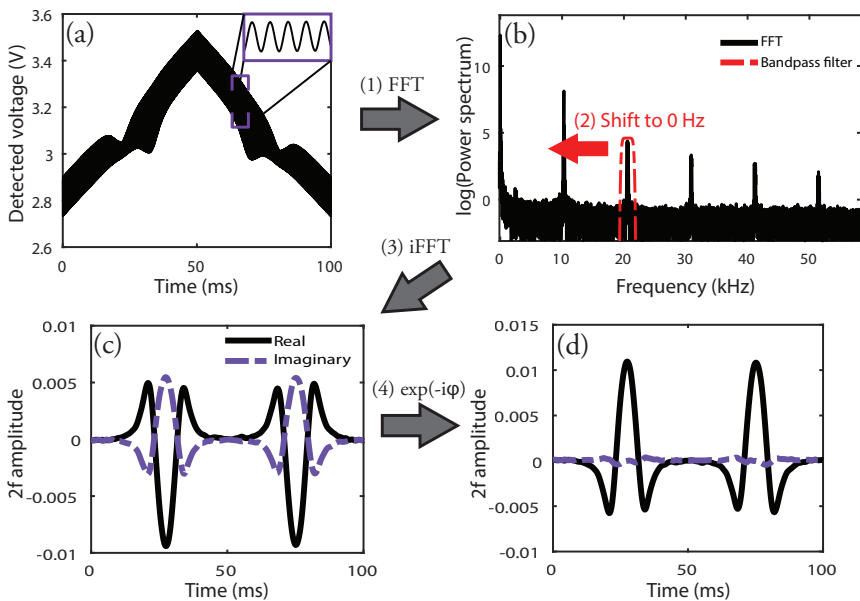
Figure 3.3: The principle of digital lock-in using Fourier analysis, is that the detected signal (a) is Fourier transformed (1) and a bandpass filter is applied to the signal in the frequency domain (b). The filter is filtering out everything except one of the harmonic of the modulation frequency (2) and the signal is then shifted to zero. Applying the inverse Fourier transform (3) results in a real and imaginary part (c). By finding out the phase at the maximum amplitude, the signal can be shifted in the complex plane (4) in order to maximize the real part of the signal (d).

Residual amplitude modulation

The diode lasers are tuned in wavelength through direct modulation of the injection current. In TDLAS, the wavelength modulated laser light is converted into an amplitude modulation when interacting with the absorption profile of a sample gas. However, the current also drives the output power of the diode laser leading to an amplitude modulation of the detected signal, I_s, even in the absence of a sample gas. This is known as residual amplitude modulation (RAM) [39] and will be introduced as a wavelength-dependent background signal, I_D, in the detected signal, i.e., $I_s(\nu) = I_D(\nu) \exp(-\alpha(\nu)L)$. Since the frequency of the light in TDLAS usually is linearly scanned in time and that the current-to-power response is linear, the RAM signal add a slope to the background signal (Fig. 3.1), which produces an offset in the 1f signal which is not presented in the 2f signal, making the recording of this one the preferred on.

3.3 Gas in Scattering Media Absorption Spectroscopy

In the special case when TDLAS is used to study gas that is enclosed into a porous, heavily scattering media, it usually goes under the name of GASMAS (Gas in Scattering Media Absorption Spectroscopy) [40, 41]. The difference from TDLAS performed in a completely gas-phase sample, is that the light impinging onto the detector has propagated through the scattering medium, experienced multiple scattering, and the propagation is distributed throughout the sample. This implies that in Eq. 2.6 the absorption path length, L_{abs}, is also a distribution of many different absorption path lenghts and the effective L_{abs} can be viewed as the mean absorption path length, $\langle L_{abs} \rangle$. When we deal with scattering media, the gas absorption path length which the light experiences will here be defined as $L_{abs} \equiv \langle L_{abs} \rangle$. It is also important to note that the optical path length through the sample is no longer equal to the absorption path length,

$$L \neq L_{abs} \tag{3.1}$$

but instead it is the sum of the absorption path length and the optical path length through the bulk material of the scattering medium,

$$L = L_{abs} + L_{bulk}. \tag{3.2}$$

In order to obtain a number density or concentration from Eq. (2.6), L_{abs} has to be known, but L_{abs} cannot easily be deduced for a scattering medium, since it is not equal with the physical length or the optical path length of the sample.

The above mentioned differences between TDLAS employed for measurements of, e.g., gas measured in cells or flows, compared to gas trapped in heavily scattering media will make the approach somewhat different. For instance, the light is usually heavily attenuated due to the absorption and scattering features of the bulk material, leading to low transmission signals. Secondly, L_{abs} is unknown and therefore alternative methods have to be introduced to get an estimate of L_{abs} which then enables evaluation of gas concentration. It should be noted that L_{abs} can in some situation be the interesting parameter to study since it can give information about material properties such as the porosity.

3.3.1 Scattering media

The scattering materials studied with GASMAS consists of two components, the gas-filled pores and the bulk material. What makes it possible to do gas-phase absorption measurement through these materials is that the absorption features of the free molecules, i.e. the gas phase, are several order of magnitude narrower than the absorption of the liquid or solid-phase bulk material itself. This is due to the broad energy level structures (Section 2.1) occuring when the atoms/molecules are packed together in a solid. For transmission of light that is scanned in wavelength over one or several absorption lines of a molecule in gas-phase, the absorption of the bulk material will simply be an essentially constant background.

An example of scattering, porous material such as wood is given in Fig. 3.4, studies on wood materials are presented in Paper I.
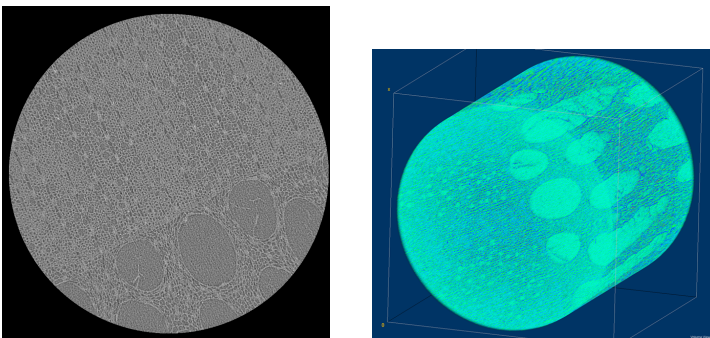

Figure 3.4: Slice of an oak imaged with X-ray tomography and to the right, the 3D reconstruction made from the slices (courtesy to Stephen A. Hall at Division of Solid Mechanics, Lund University for providing the images). The dark areas represent the pores.

3.3.2 Absorption pathlength determination

As mentioned previously, both the optical and absorption path length of light propagating through a porous material are unknown and do not correspond to the physical length of the sample. In order to evaluate a number density or concentration from Eq. 2.6, the absorption path length has to be known. In this thesis, the absorption path length has been estimated using primarily two different methods.

The first method relies on performing a reference measurement in a gas volume where the concentration and absorption path length are known. It is of course important to note that the same transition wavelengths are used in the reference as is used in the sample measurement. The absorption signal obtained from the sample is then fitted to the reference signal and a scaling coefficient is obtained. In the case that both the concentration and absorption path length are unknown, an absorption path length is obtained that corresponds to the absorption experienced if the light would be propagating through the sample with a concentration of absorption gas that is equal to the concentration in the reference measurement. This absorption path length is usually called the *equivalent (mean) absorption path length* and when the concentrations are equal, the equivalent mean absorption path length is equal to the mean absorption path length. This is useful when performing WMS, since the exponent in Eq. 2.6 cannot directly be obtained but is proportional to the 2f signal.

The second method is to employ a dual-wavelength setup for the case when the gas mixture contains a molecule with known concentration. Then measuring the absorption for that transition, the absorption path length is obtained and can then be used in the calculation of the concentration of the molecule of interest. Since two wavelengths are employed, one for each transition, this method assumes that the optical path length is equal for the two wavelengths. This approximation becomes less valid the larger the difference between the two wavelengths is. This method has been employed in Paper IV, where the temperature was monitored and from a relative humidity of 100 % in the lungs, the water vapor concentration was calculated and then the absorption path length could be obtained by measuring the water vapor absorption at 820 nm.

Chapter 4

Medical applications

A part of this PhD project has been participation in a EU-project called Neo-lung [42], where the aim was to, together with industrial partners, develop a prototype system for real-time, non-invasive monitoring of the lungs of preterm infants based on the GASMAS technique (covered in Sect. 3.4). In Fig. 4.1, an overview of the project is presented where the author's involvement can be divided into three phases. The first phase was to develop an optical phantom for system evaluation. The second phase was to perform a pre-clinical trial on anesthetized piglets. The last, third phase, was a clinical trial on healthy newborn infants. These phases will be described in more detail in the following sections.

Project overview

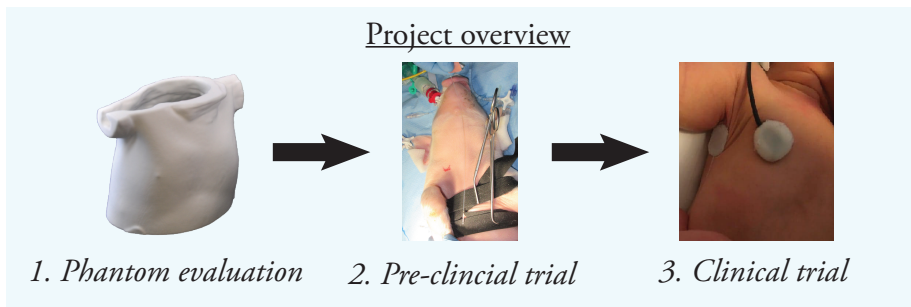1. Phantom evaluation   2. Pre-clincial trial   3. Clinical trial

Figure 4.1: Short overview of three phases in the project, with the aim to develop a tool for non-invasive gas content monitoring in the lungs of preterm infants.

4.1   Background

Premature infants, which are defined as babies born earlier than 3 weeks before the normal period of 40 weeks, suffer an increased risk of both short- and long-term health complications due to underdeveloped organs [43]. Early symptoms can for example be difficulties to keep a constant body temperature or breathing trouble. The earlier gestational age, the more underdeveloped organs and thereby increased risk for health complications. At birth, the preterm infant may be treated at a neonatal intensive care unit, placed in an incubator where the body functions are monitored and medical support is provided.

The lung is one of the underdeveloped organs, and results in breathing difficulties for the preterm infant. The preterm infant may suffer from the respiratory distress syndrome (RDS), which is caused by underdeveloped lungs and insufficient amount of pulmonary surfactant. The surfactant [44] is a liquid coating the alveoli that, somewhat simplified, reduces the surface tension and makes it possible for the alveolus to inflate and deflate. Without sufficient amount of surfactant, the pressure difference makes the alveoli prone to collapse. Pulmonary surfactant starts to develop at week 26 of gestation. However, sufficient surfactant amounts are not generated until week 35 of gestation [45]. The condition may lead to long-term respiratory problems known as Chronic Lung Disease (CLD) or Bronchopulmonary Dysplasia (BPD) [46, 47], due to lung injury caused by mechanical ventilation and too high inspired oxygen concentration during medical support.

Careful use of oxygen and mechanical ventilation, and use of surfactant replacement can prevent BPD [48]. The increasing survivability for preterms born in earlier gestational age, thanks to advances in modern medical science, has also lead to an increase of lung disorders.

The golden standard for diagnosis of lung disorders in preterm infants is chest X-ray imaging. The use of X-ray radiation at the neonatal intensive care unit on the preterm babies provides a snapshot of their lungs and is crucial in diagnosis. However, the radiation is highly energetic (100 eV - 100 keV) and ionizing. It is documented [10] that preterm infants exposed to X-ray radiation will have an increased risk of developing malignant tumors in their adult life.

Reducing the use of X-ray radiation at the neonatal intensive care units by implementation of the GASMAS technique, is the motivation for the project mentioned in the previous section. The GASMAS technique uses radiation in the visible to the near-infrared parts of the electromagnetic spectrum, which means that it is possible to obtain gas information in a way that is non-invasive. The drawback with the GASMAS technique compared to the use of X-rays is that it

is not an imaging technique and that the detected light has been multiply scattered, meaning that it is challenging to extract exactly from where in the lung the gas absorption signal is originating. What is instead gained is the potential to obtain both gas and lung volume information, non-invasively and with continuous monitoring. The project aim has been to investigate the potential of the GASMAS technique towards 24h monitoring of preterm infants at neonatal intensive care units.

4.2 Light transmission in tissue

As mentioned, the GASMAS technique utilizes the fact, that the absorption features of the gas embedded in the scattering medium are several orders of magnitude narrower than those of the surrounding tissue, as shown in Fig. 4.2. Human, or more generally, animal tissue, i.e. the bulk material of the porous scattering medium, is a complex structure, and light that has propagated through tissues is attenuated based on the absorption and scattering properties of the different tissue components. The values of the optical constants characterizing the tissue can be found in various literature. However, one of the main challenges is the variation in optical properties reported by different groups [49], mostly originating from the large variation in tissue between individuals.

The dominating chromophores that influence the absorption behavior of tissue are blood and water due to their relatively high concentrations. Water is transparent in the so called optical window between roughly 650 nm and 1200 nm, while its absorption is instead dominating in the near-infrared region and also at deep UV wavelengths. Blood mainly consists of blood plasma and red blood cells. Blood plasma contains around 90 % water and the rest is made up by different proteins and trace molecules [50, 51]. The hemoglobin in the red blood cells gives blood its color and is responsible for binding molecular oxygen and transport it out to the cells in the body. Hemoglobin is mostly absorbing at wavelengths below 600 nm (Fig. 4.2a). The absorption profile of hemoglobin is slightly different depending on if the hemoglobin has bound oxygen or not. This is used in pulse oximetry [52] to measure the oxygen saturation in the blood.

Obtaining gaseous oxygen concentrations

The oxygen concentration is calculated from the measurement of the calibrated absorption of oxygen (O_2) and water vapor (H_2O). The water vapor concentration is obtained by measuring the temperature and pressure. The saturation vapor
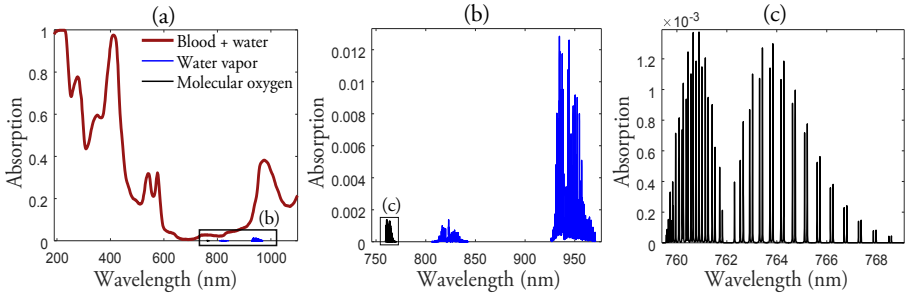
Figure 4.2: Transmission measurement through a 10 mm cell containing approximately 0.3 % red blood cells and 99 % water (red line) (a), the rest is made up of molecules from the plasma. In comparison, absorption of gaseous water (blue line) and oxygen (black line) (b) was simulated for an absorption path length of 10 mm and further magnification show the narrow absorption features of the absorption band of oxygen (c).

pressure, P_s, is obtained from a polynomial expression (Eq. 4.1) [53], depending on the temperature, T[K], and where P_A is the standard atmospheric pressure.

$$P_s(T) = P_A e^{13.3185t - 1.9760t^2 - 0.6445t^3 - 0.1299t^4} \tag{4.1}$$

$$t = 1 - \frac{373.15}{T} \tag{4.2}$$

By knowing the saturation vapor pressure, the relative humidity and the atmospheric pressure, the water vapor concentration can be obtain from the ideal gas law, i.e. $N_{H_2O} = RH * P_s/P$, where P is the air pressure. From the measurement of the water vapor absorption and calculating the water vapor concentration, the absorption path length, L_{abs}, is obtained. Note that the absorption is calibrated so that it is given in the unit [%m]. It is assumed or approximated that the absorption path length is the same at the wavelengths where oxygen and water vapor are absorbing,

$$L_{abs}(\lambda_{O_2}) = L_{abs}(\lambda_{H_2O}). \tag{4.3}$$

From this substitution it is possible to calculate the oxygen concentration from the measured absorption of O_2, Abs_{O_2}, and the absorption path length of H_2O:

$$N_{O_2} = \frac{Abs_{O_2}}{L_{abs,O_2}} = \frac{Abs_{O_2}}{L_{abs,H_2O}} = \frac{Abs_{O_2}}{Abs_{H_2O}} N_{H_2O} \tag{4.4}$$

Since the scattering properties are wavelength dependent, the absorption path length will be dependent on the light transmission through the scattering medium

and therefore also be wavelength dependent. Therefore, the smaller difference in wavelength the better the approximation in Eq. 4.3 will be. That is the main reason why in later works, Paper III and IV, the water vapor absorption at 820 nm was used together with the O_2 absorption band at 760 nm (Fig. 4.2c), even though the absorption cross section at 820 nm is lower compared to 935 nm (Fig. 4.2b), which was used in the early Paper II.

4.3 Phantom models for system evaluation

One of the many challenges for evaluating spectroscopic techniques in medical applications is the lack of or the difficulty to get access to measurement samples. Instead, phantoms created with optical properties similar to those of real tissue are used for evaluating techniques or dose distributions. Optical phantoms can be in the form of liquids or slabs, when the optical properties are the main target of investigation and the geometrical form is of less importance. Lately, the increased availability of 3D-printers has impacted the field of biophotonics with the possibility to create optical phantoms with complex shapes and materials. Gypsum and silicone models of the thorax for kilovoltage X-ray [54], breast phantoms for tumor detection using ultrasound and MRI [55], plastic lung model for CT imaging [56], and head phantom for MRI studies [57] have been constructed. There is also an increase in printed implants using biomaterials [58], and recent advances in 3D-printing show improved phantoms for surgical training [59].

A set of CT images of the thorax of a 13 days old preterm infant, born at a gestational age of 33 weeks, with a weight of 1300 g was obtained from the Skåne University Hospital. The images were provided in the DICOM (*Digital Imaging and Communications in Medicine*) format, which is an international standard to store and display medical images. The images were visualized using the free software NIRFAST [60, 61]. NIRFAST was also used for segmenting the images and the program also provides near-infrared light transport simulations, which were performed on the segmented 3D model [62].

4.3.1 3D-printed phantom

The segmentation of the CT-images was handled in NIRFAST, and to reduce the complexity, six tissue groups were identified and each group was treated as being homogeneous in the sense that each tissue group was allocated an absorption coefficient and a reduced scattering coefficient. After segmentation, the 3D-model was divided into the regions heart, bone, lungs, muscle, skin and fat. Since the

printing was done using the material nylon (white), it was decided to only print the boundaries of the different regions and then create liquid phantoms to fill the different regions since the nylon material poorly represents optical properties of the different tissues. The liquid phantom contained a mixture of Intralipid®, Indian ink and water, which enable manipulation of the absorption and scattering properties of the liquid.

The first version of the optical phantom was 3D printed using the laser sintering technique. The boundary or the surface was printed with an average thickness of 0.6 mm, which was found to be the smallest possible thickness to avoid leaking or deforming the 3D printed structure. The phantom was printed in four components. The skin was printed with a double layer (Fig. 4.3a) which can contain the liquid fat phantom. The bones (Fig. 4.3b), i.e. the ribcage and spine were printed solid, since nylon has a high scattering coefficient. The lungs (Fig. 4.3c), with the interconnecting trachea were printed hollow. Lastly, the heart (Fig. 4.3d) was printed single-walled and was later filled with the heart liquid phantom.
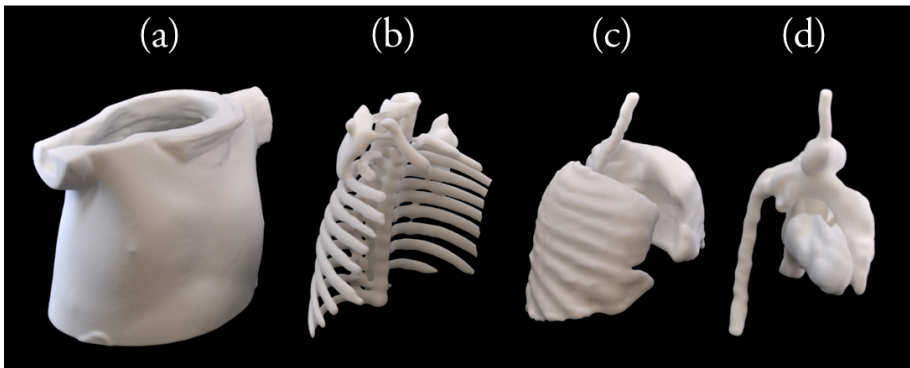
Figure 4.3: The 3D printed optical phantom with the different components, (a) thorax i.e., the skin and container for the fat and muscle phantoms, (b) the bone structure, (c) the lungs and (d) the heart. Note that the different components are not shown in scale.

4.3.2   Liquid phantom

The liquid phantom was created by mixing Intralipid® and Indian ink diluted in water. This mixture is frequently used to create phantoms in the field of medical optics. The reason is that Intralipid® is characterized by a very large scattering

coefficient and a very low absorption coefficient. On the contrary, Indian ink has a large absorption but low scattering coefficient. Adjusting the relative concentrations of the liquid, it is possible to tailor the optical properties, i.e., the absorption and scattering coefficients. When the liquid phantoms had been created (Table 4.1), they were filled into the 3D-printed phantom as can be seen in Fig. 4.4. The ink eventually discolored the nylon if contained for too long and the Intralipid® continuously degrades and therefore the liquid phantoms were never kept for more than 24 hours (in room temperature).

Table 4.1: Absorption, μ_a, and reduced scattering, μ'_s, coefficient of the different liquid phantom evaluated with time-of-flight spectroscopy.

	763 nm		820 nm	
Tissue phantom	μ_a	μ'_s	μ_a	μ'_s
Muscle	0.34	7.96	0.31	7.22
Heart	0.38	5.43	0.34	4.77
Fat	0.13	10.14	0.14	9.21

Figure 4.4: Picture of the 3D-printed phantom with the liquid phantom filled into the hollow organs.

4.3.3 Experimental setup

The 3D-printed phantom was evaluated using mainly two different GASMAS systems. In the work presented in Paper II, a laboratory system was used, while a GASMAS system provided by the project partner GPX-Medical was used in the work reported in Papers III and IV. The systems were based on the same principles and had similar designs overall (Fig. 4.5). Two diode lasers, with emitting wavelengths for measuring absorption from molecular oxygen and water vapor, had their light beams superimposed and directed into an optical fiber. In the laboratory system a bifurcated fiber was used to superimpose the two beams, while in

the other system a beam splitter was used, whereupon the two beams were focused into an optical fiber. The light transmitted through the optical fiber was delivered, in the first version, from the bare fiber end. Later in the project, the bare fiber end was replaced with a diffuser, as described in Paper III. The main reason for using a diffuser is to achieve lower exposure to the laser light and avoid heating effects on the skin.
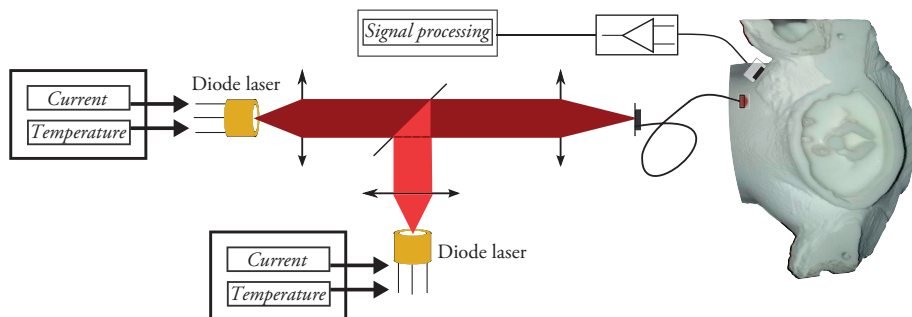

Figure 4.5: Schematic drawing of a general experimental setup for evaluating oxygen concentration using a GASMAS system. Two lasers are employed to measure absorption of molecular oxygen and water vapor in the gaseous volume. A photodiode is collecting the transmitted light and the signal from the detector is amplified through a trans-impedance amplifier before signal processing, which can be done with both hardware and software.

The light that has penetrated through the optical phantom is collected by a detector. In this work silicone (Si) photodiodes with an area of 1 cm^2 have been used. In principle, detectors such as avalanche photodiodes or photo multiplier tubes (PMT) can also be used, especially in applications with low light transmission. However, since these detectors involve high voltage they are not desirable in medical applications where the detector needs to be in contact with the skin of the patient. When considering babies and preterm infants this aspect is even more crucial.

The signal from the detector is amplified using a trans-impedance amplifier (TIA) before being recorded. In the laboratory system a data acquisition card (National Instruments) was used and controlled through the program LabView (National Instruments).

4.3.4 Phantom evaluation

Phantom measurements - different lung models

In the work reported in Paper II, the lung model used was hollow and filled with air. The absorption path lengths obtained from measurements on this lung model were relatively large compared to those obtained in an earlier clinical trial on healthy full born babies [11], with absorption path lengths up to 10 cm. This was possibly due to a combination of a large gas volume and reflections inside the hollow lung. This was later modified by introducing a sponge material into the lung model, with the main purpose to reduce the gas volume and have substantially more scattering and absorption in the model, i.e., representing conditions that better resemble those in a real lung.

The possibility to accurately measure oxygen concentration is based on the water vapor concentration being calculated, which is an assumption that requires information about the relative humidity and temperature of the gas volume. Since the real lung is wet and almost a closed cavity, it is assumed that the gas contains water vapor with a relative humidity of 100% and a temperature corresponding to the surrounding tissues. This was achieved partly by the sponge material, to which a few drops of water were added to make it moist, and the slow diffusion of water through the nylon walls of the 3D-printed lung.

Phantom measurements - light source and detector positions

The different phantom models were investigated by positioning the light source and detector on the skin. The different positions are shown in Fig. 4.6a and 4.6b, and were distributed both on the front and the back of the 3D-printed model, as well as under the right and left armpit. The positions were constrained by the size of the detector and light source, and by the shape of the phantom. In order to remove possible air pockets between the skin of the phantom and the laser source or detector due to the uneven surface, ultrasound gel was applied in between. If the light would have propagated through these air pockets, it would introduce an undesired offset in the resulting absorption signal.

With the hollow lung model, by placing the detector, e.g., under the right armpit (AR), a detectable absorption signal was obtained when the detector was placed on the right hand side of the model (Fig. 4.6c). Signal was obtained both at the front and back of the model, but the detected light intensity was much weaker when the detector was placed on the back (Fig. 4.6d). Mirrored results were obtained when placing the detector under the left armpit, but due to the heart,

the detected intensity was ten times lower for the detector positions on the front of
the model. It should be noted that, in this case, no detectable signal was obtained
for detector positions on the opposite side of phantom to the light source, e.g.
detector under the right armpit and the light source positioned on the left side of
the phantom.
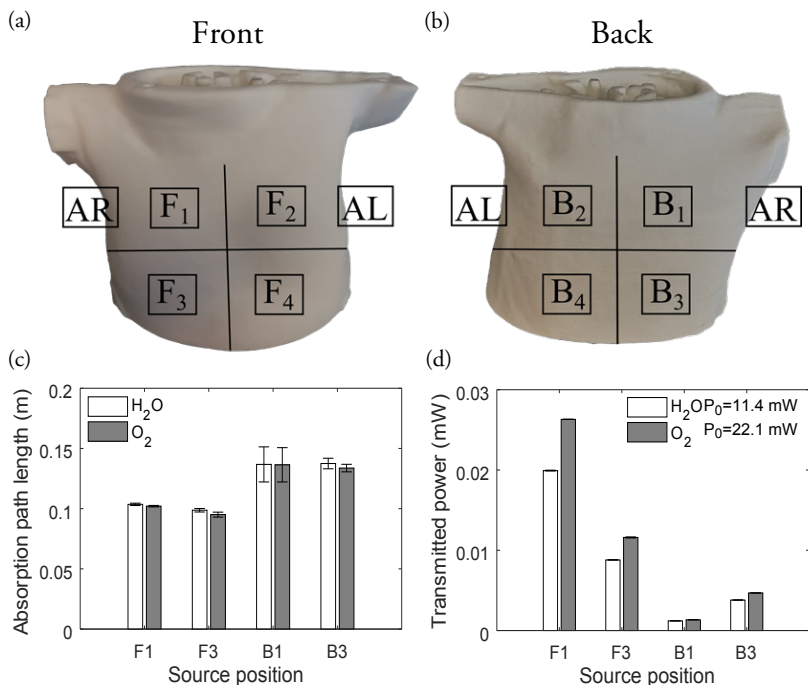
Figure 4.6: Positions on the hollow lung model for the light source and detector at the
front (a) and back (b). Measured absorption path lengths for different laser source posi-
tions with the detector located under the right armpit (AR) are shown in (c). Panel (d)
shows the corresponding transmitted laser power.

As mentioned in the previous section, the absorption path lengths obtained
are relatively large when comparing to what is expected in real lungs. The study
was repeated on the improved lung model, with the laser source placed under the
armpits. Compared to the hollow lung model, the absorption path lengths became
shorter and the transmitted intensity was also reduced. It is difficult to evaluate
how much of the light that did not travel through the lung, since the absorption
signal obtained from the GASMAS technique is only sensing the absorption path
length through the gas volume. However, detected light that has not propagated

through the gas volume will reduce the mean absorption path length through the sample. It is possible to obtain the total optical path length, i.e. the sum of the gas absorption path length and the path length through the bulk, by employing techniques utilizing time-of-flight [63] and phase shift [64] measurements.

Internal light illumination

Disadvantages with source-detector positioning on the skin, discussed in the previous section is that part of the light being collected on the detector has not passed through the area of interest, i.e. the gas volume in the lung. Furthermore, the detected light that carries gas information must first propagate to the lung, from the source, and then back to the detector, experiencing heavy attenuation in both cases. An alternative approach is to use an optical fiber that would then be inserted into the trachea (windpipe) or the esophagus (foodpipe). This approach would still be non-invasive in the sense that preterm infants at the neonatal intensive care unit are usually fed through a nasogastric tube or are mechanically ventilated with an endotracheal tube inserted into the trachea.

    This approach was tested on the phantom and an optical fiber with a diffuse end was used. It was inserted into the phantom at two positions, the first position being into the 3D-printed trachea (as shown in Fig. 4.7) and the second position into the liquid phantom, at a position just behind the trachea, representing the position of the esophagus. It should be noted that the esophagus was not 3D-printed so an approximated position was used, based on anatomical images and assessment by a medical expert.
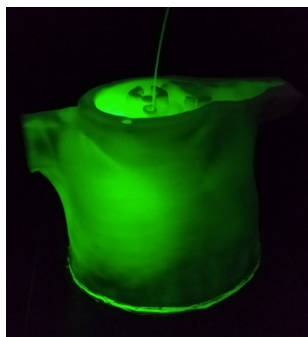

Figure 4.7: Picture taken with an optical fiber inserted into the trachea of the 3D-printed phantom. Here a green laser pointer is used for the purpose of demonstration.

    Delivering the light internally using an optical fiber removed one practical

difficulty that usually is present in the GASMAS technique, namely that the light observed by the detector has indeed been transmitted through the model, rather than via light paths outside the model, e.g., due to leakage between the light source and the detector. A comparison between internal and dermal (on skin) illumination with the detector placed under the right armpit is shown in Fig. 4.8. As can be seen in the figure, internal illumination (Trachea and Esophagus) results in longer absorption path lengths than dermal illumination (F_1 and F_3). This increase could be due to the fact a larger portion of the detected light has been transmitted through the lung instead of propagating through the liquid phantom.

The oxygen concentration was also evaluated using the water vapor absorption band at 820 nm and the method described in Sect. 4.2. The water vapor concentration was calculated by assuming a relative humidity of 100% and the temperature was measured by placing a thermometer into the liquid muscle phantom. The results are promising, especially compared to the study based on measuring the water vapor at 935 nm.
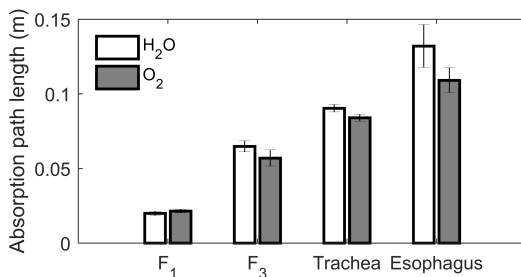
Figure 4.8: The absorption path length measured at 760 nm (O_2) and 820 nm (H_2O) for the detector placed under the right armpit of the 3D-printed model. The light source was positioned at the right half of the front of the model (F_1 and F_3) and the optical fiber was inserted into the model corresponding to positions of the trachea (windpipe) and the esophagus (foodpipe).

4.4   Pre-clinical studies

The pre-clinical study was performed at the Rigshospitalet in Copenhagen, Denmark. The study was pursued on anesthetized Danish Landrace piglets and was approved by the Danish Animal Experiments Inspectorate. During the experiment, the piglets were handled by qualified medical doctors following the guidelines outlined by FELASA (Federation of European Laboratory Animal Science

Association) [65]. The accepted measurement protocol included performing studies evaluating both dermal (Fig. 4.9a) and internal illumination (Fig. 4.9b) for stepwise change of inspired oxygen concentration, i.e., the set value of the oxygen concentration on the ventilator connected to the piglet, and to induce a limited number of the lung complications pneumothorax and atelectasis (see next section for further details).

(a)   (b)   (c)
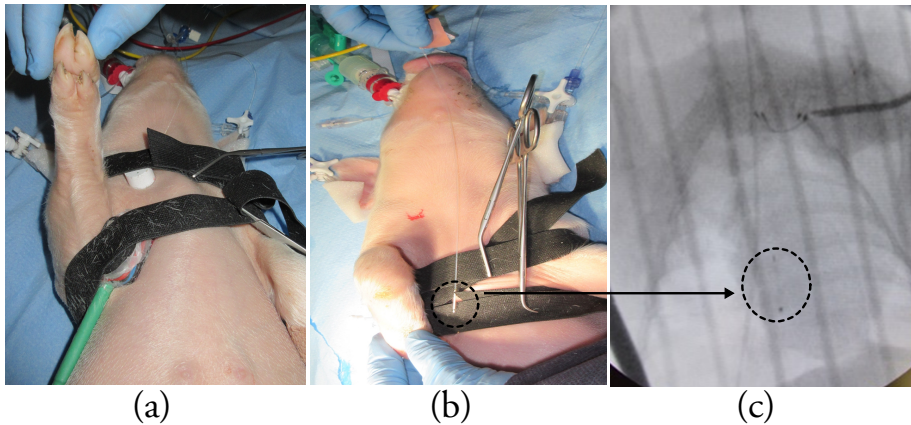
Figure 4.9: (a) The picture shows the anesthetized piglet with the detector placed under the right foreleg. The dermal light diffuser can be observed being placed just above the detector. (b) This picture shows the optical fiber used for internal light illumination from the esophagus (foodpipe). The last centimeter of the optical fiber is diffused (black dotted circle). (c) Markings (black dotted circle) on the optical fiber made it possible to locate its position using X-ray imaging.

4.4.1 Lung physiology

Since most readers of this thesis probably will have, just as the author, a background different from medicine, a brief overview of the respiratory organ and function will be presented in this section. A more complete and complex description of the organ can be found in various literature [44].

The air is initially transported in the lungs through the trachea (also called windpipe). The trachea then divides into the right and left main bronchus, followed by 22 further generations of divisions before the air reaches the alveoli where gas exchange occurs. Human lungs consist at peak performance of around 300 million alveoli, with a total surface area of around 80 m^2. It is in the alveoli where

O_2 and CO_2 exchange, through a thin respiratory membrane between the lung and the blood in the capillaries surrounding the alveoli.

The driving force of air exchange is a pressure gradient between the air in the lung and the blood, i.e., the blood transported from the heart into the lung is deoxygenated and the partial pressure of O_2, P_{O_2}, is lower than the P_{O_2} in the lungs. This pressure gradient enables diffusion of oxygen into the blood where it will bind, weakly, with an iron atom in the hemoglobin and then transported out to the cells in the body. Similarly, the CO_2 created in the body cells is transported through the blood and due to a higher blood P_{CO_2} it diffuses out into the air in the alveoli. Since diffusion through the respiratory membrane is not constrained to only O_2 and CO_2 molecules, exhaled gas can be analyzed to detect trace molecules connected to diseases, e.g. acetone can be a biomarker for diabetes and increased concentrations of ammonia can be an indication of liver disease [66, 67].

Air is inspired actively and exhaled passively. During inspiration the diaphragm (the main breathing muscle located just below the lungs) contracts, expanding the lung. The increased volume lowers the pressure and the higher atmospheric pressure forces air down into the lungs. During exhalation the lung volume is instead decreasing which passively pushes the air out of the lung. Due to the moist surface of the alveoli, the surface tension due to the water molecules makes it difficult for the alveoli to inflate when the next breath is initiated, and they can even collapse. That is why some alveoli cells produce pulmonary surfactant which reduces the surface tension and makes it possible for the alveoli to inflate and deflate. A surfactant deficiency often occurs for preterm infants, as discussed in Sect. 4.1. Other lung disorders, such as pneumothorax and atelectasis, which can hinder respiration, will be discussed in the next section.

Pneumothorax and Atelectasis

Pneumothorax is the collapse of the lung due to air leaking into the pleural cavity (the area between the chest wall and the lung). One of the functions of the pleural cavity is to keep the lung expanded by exerting a negative pressure. When, for example, the outer membrane to the chest wall becomes punctured, atmospheric air is filling the pleural cavity and the lungs can partly or fully collapse, leading to breathing difficulties.

Atelectasis is also a form of lung collapse, which occurs due to that the alveoli collapse and may also have different causes. If the bronchus is obstructed, e.g., by blood or mucus, the air in the lung will be reabsorbed, resulting in the collapse of the alveoli. Insufficient amount of surfactant to reduce the surface tension of the

alveoli can also lead to atelectasis, which may arise in preterm infants where the surfactant yet has to be fully developed.

4.4.2 Oxygen concentration evaluation by varying inspired concentrations

The piglets were supported with oxygen through a respirator, where the fraction of inspired oxygen (FiO_2) could be manually adjusted. The respirator also provided information about the fraction of inhaled and exhaled O_2 and CO_2, tidal volumes, and breathing frequency.

The main aim of the study was to evaluate the oxygen concentration with the GASMAS technique and therefore the FiO_2 was set for values FiO_2 = (0.25, 0.3, 0.5, 0.75, 1.0). For each value of FiO_2 the absorption due to O_2 (Fig. 4.10a) and H_2O (Fig. 4.10b) was measured by switching between the 764 nm and 820 nm diode laser. The measurements were performed for two light source and detector geometries: 1) both the diffuser and the detector were placed on the skin, i.e., dermally, and 2) with internal light illumination, where the laser light was delivered through an optical fiber with a diffuse end and the optical fiber positioned into the esophagus (food pipe) of the piglet. In both cases, the detector was positioned just below the right foreleg of the piglets (Fig. 4.9a). Evaluating an oxygen
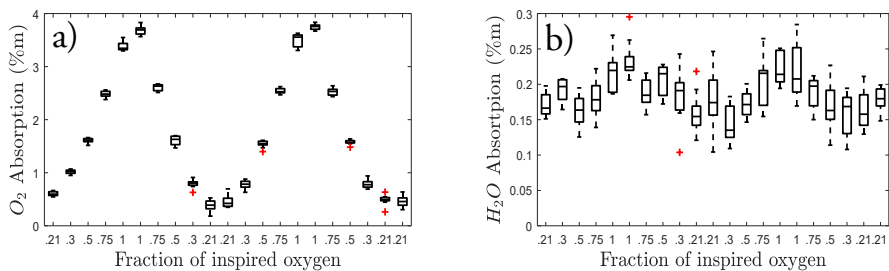
Figure 4.10: Absorption from O_2 (a) and H_2O (b) with the light source positioned in the esophagus of the piglet and the detector below the right foreleg. The data represent a full measurement series where the value of the oxygen concentration of the ventilator was stepwise increased and decreased between 21 % and 100 %. The boxplots show the median, the 25th and 75th percentiles, extreme values and outliers (red cross).

concentration for a dermal measurement geometry was in most cases not possible due to an absent H_2O and a low O_2 signal. The reasons were partly due to low laser power of the 820 nm diode laser which measured an output power of 8.1 mW from the optical diffuser, and the fact that the absorption cross section for H_2O at 820 nm is on the same order as O_2 at 764 nm (Fig. 4.2b) but at a lower

concentration of around 6.5 %. The concentration was obtained by assuming a relative humidity of 100 % at a body temperature of 38 °C. It should be noted that pigs have a slightly higher normal body temperature than humans.

The GASMAS measurements performed with the internal light illumination were performed on five piglets. For each value of FiO_2 the signal was averaged for 10 s and repeated 8-12 times. From the measured absorption of O_2 and H_2O, together with the measured body temperature performed with a rectal thermometer, the O_2 concentration (Fig. 4.11) was calculated using Eq. 4.1. Since the absorption from O_2 and H_2O were not collected simultaneously, but sequentially by switching between the 764 nm and 820 nm diode laser, the data sets were not considered paired. The data was instead treated by taking the median of the H_2O absorption and using that in Eq. 4.1 to calculate the concentration for that set value of FiO_2. This was done in order to be able to perform ANOVA tests in the program MATLAB. ANOVA tests if the means of data sets are equal. When
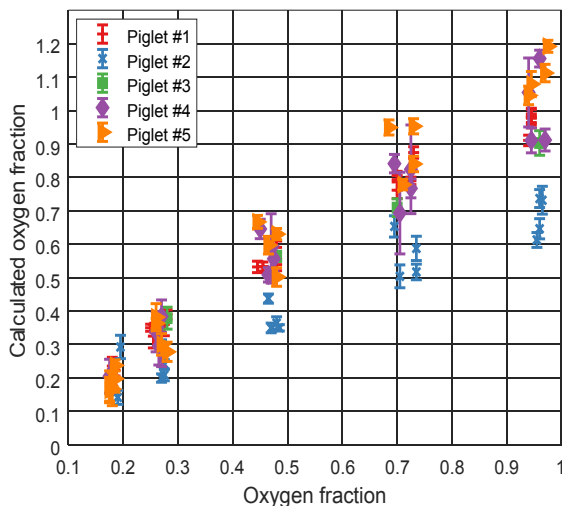
Figure 4.11: The calculated oxygen fraction, presented with a mean and standard deviation, from the GASMAS measurements on the five piglets with internal light illumination through the esophagus. The oxygen fraction was obtained by taking the mean of the inhaled and exhaled oxygen fraction measured by the oxygen ventilator.

performing the ANOVA test, the data were grouped according to the FiO_2 setting on the oxygen ventilator and it was observed that there was a significant difference (P«0.05) between the means of the FiO_2 values. However, when taking into account the individual piglets, there are clearly overlap between different FiO_2 (Fig.

4.11) and the spread is relatively large. Unrealistic values of the O_2 concentration were also obtained, i.e., over 100 %, which can be due to etalon fringe effects contaminating the optical signals, and hence the evaluated data, and invalid assumptions of the relative humidity and equal absorption path length at 764 nm and 820 nm.

4.4.3 O_2 absorption monitoring during induced lung complications

In the pre-clinical study, lung collapse was induced on the right lung where the dermal detector was positioned. Pneumothorax was induced by injecting air into the pleural space, and air was subsequently sucked out to re-stabilize the lung. Atelectasis was created by physically blocking one of the bronchii using a small inflatable balloon. Since the measurement system did not allow simultaneous detection of both O_2 and H_2O absorption, only the O_2 absorption was measured.

Pneumothorax

Pneumothorax was performed on four subjects and performed three times in each subject. The whole procedure took around 15 minutes, and during this time the oxygen concentration was set to 100 % and the injected air into the pleural space contained 21 % O_2. When pneumothorax was initiated an increase of detected light transmission and a decrease of O_2 absorption were observed (Fig. 4.12). This is explained by the fact, that when atmospheric air is injected into the pleural cavity, an eliminated negative pressure in the pleural cavity makes the lung collapse and the O_2 absorption observed during pneumothorax then originates from the gas in the pleural space. The lung collapse also increases the transmission of light, probably due to less absorbing tissue in the optical path.

Atelectasis

When inducing and observing atelectasis, the lung was ventilated with an oxygen concentration of 30 %. During atelectasis, both the O_2 absorption signal and the light transmission were found to decrease (Fig. 4.13). However, the decrease was not as prominent as in the case when pneumothorax was studied, and it was also decreasing over a longer time. The observed decrease of O_2 absorption can partly be associated with the consumption of O_2 while the blocked bronchii prevented resupply of O_2 to the lung. It may also be due to a physical change of the lung structure, resulting in a smaller gas volume due to atelectasis, which is supported by the observed decrease of light transmitted through the lung during atelectasis.
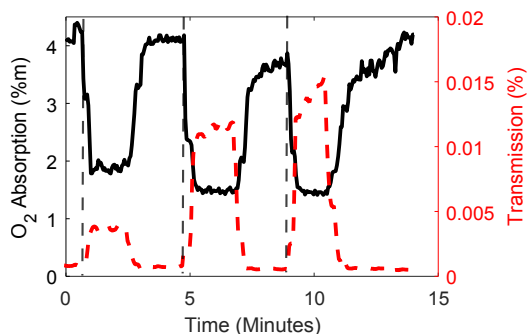
Figure 4.12: Pneumothorax repeated three times (grey dashed line) in one piglet by injecting air into the pleural space while the lung was ventilated with 100 % O_2.
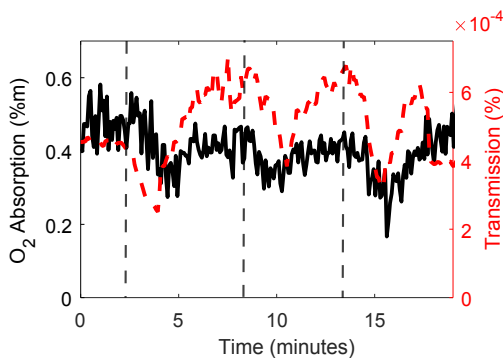
Figure 4.13: Atelectasis repeated three times (grey dashed line) in one piglet by inflating a balloon in the right bronchus. The lung was ventilated with 30 % O_2.

4.5   Clinical trial

At the Skåne University Hospital in Lund, a clinical study was performed at the "Patienthotellet", where healthy newborn babies and their mothers can stay for a few nights. The GASMAS system, used in the previous pre-clinical study, was used to measure the oxygen content in lungs of newborn, i.e. less than 24 hours old, babies.

The measurement protocol was to measure at six different source and detector positions, with the detector placed under the right and left armpit and the light diffusor placed at six position on the thorax of the baby. A total of 12 babies weighing between 2.9-4.1 kg where participating, and 11 went through the complete measurement protocol. The detector and diffusor were updated versions

from the pre-clinical study and were attached to the skin using a double-coated adhesive tape that is medically approved and used clinically for pre-term infants.

Similar to the pre-clinical study, it was difficult to obtain any signal using the dermal measurement geometry and many of the positions did not give any detectable signal. In Fig. 4.14a, the signal-to-noise ratio (SNR) of the O_2 absorption signal is presented, measured at a position on the right side of the infant just below the nipple level. The SNR was calculated by dividing the amplitude of the signal with the amplitude of the background signal (Fig. 4.14b). The low SNR was mainly due to interference fringes or etalons (Fig. 4.14b).
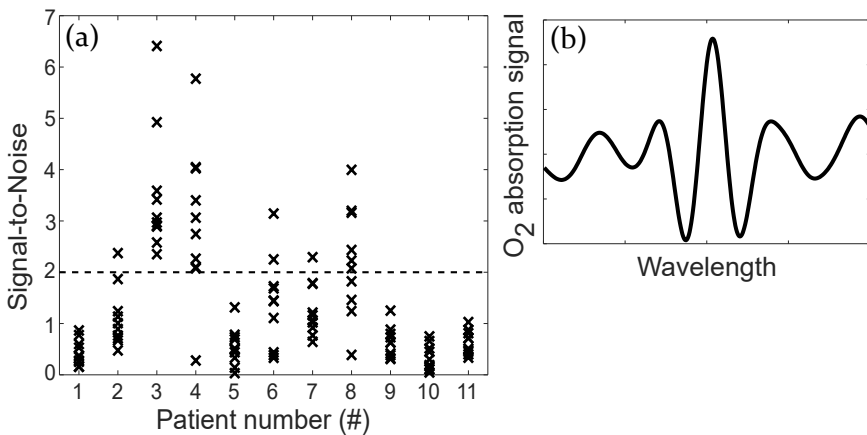

Figure 4.14: (a) Evaluated signal-to-noise ratio for the 11 infants when the O_2 absorption signal (cross) was measured at the same position on the right side of the thorax. (b) Measured O_2 absorption signal representing a signal-to-noise ratio of 2.

Chapter 5

Environmental monitoring

Monitoring of the atmosphere has in this thesis work been done with the Lidar (Light Detection and Ranging) technique, where laser light is transmitted into the atmosphere and the backscattered signal from molecules and particles in the air is collected. Range information is normally obtained by measuring the time delay between the emitted laser pulse and the detected echo signal. The laser pulse width is commonly of the order of $\sim$ns. In the work presented in Papers V and VI, continuous wave (CW) diode lasers have been used in a technique called Scheimpflug Lidar, which is a method, where the range is angular resolved and focus is achieved along the full laser beam by fulfilling the Scheimpflug condition and the Hinge rule [16]. In short, if the laser beam and image plane are non-parallel, focus can be achieved by tilting the lens plane so that the three planes intersect. However, to ensure that the object plane (laser beam) is in focus, the Hinge rule also has to be obeyed, which states that the object plane, front focal plane and the plane going through the lens while parallel to the sensor have to intersect (Fig. 5.1).

Scheimpflug Lidar allows the use of relative inexpensive CW diode lasers with high average power and has been used for monitoring of, e.g., fauna [68, 14], aerosols [69] and combustion processes [16]. In the work presented in Paper V, two CW lasers, of 980 and 1550 nm wavelength, respectively, were employed for studying particle releases in the atmosphere, and the signals at the two wavelengths were compared observing that backscattering behaves differently for different particles and wavelengths.
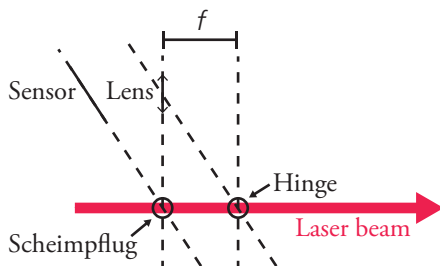
Figure 5.1: Illustration of the geometry in a Scheimpflug configuration. The dashed lines represent the image, lens and front focal planes. Focus along the laser beam (object plane) is achieved when the planes intersect at the Scheimpflug and Hinge lines.

5.1   Differential absorption Lidar

The main principle of differential absorption Lidar (DIAL) is that two laser beams with different wavelengths that are on, λ_{on}, or off, λ_{off}, an absorption line of the species of interest, are used when measuring the backscattered signal.. It can be compared to TDLAS, but with the important difference that the obtained signal is range resolved. This makes it possible to obtain the absorption coefficient (Eq. 2.6) by dividing the backscattered signals $P(\lambda_{off}, r)$ and $P(\lambda_{on}, r)$, and then taking the range derivative. The DIAL equation for evaluating the number density of a probed gas species, with absorption cross sections σ_{on} and σ_{off} at the wavelengths λ_{on} and λ_{off}, respectively, then becomes Eq. 5.1. Dividing the expression by two is necessary since the light travels twice the measured distance. The background problems encountered in TDLAS cancel out in DIAL when the two signals, $P(\lambda_{off}, r)$ and $P(\lambda_{on}, r)$, are divided by each other:

$$ N_X = \frac{1}{2(\sigma_{\lambda_{on}} - \sigma_{\lambda_{off}})} \frac{\mathrm{d}}{\mathrm{d}r} \ln \left(\frac{P(\lambda_{off}, r)}{P(\lambda_{on}, r)} \right) \tag{5.1} $$

In the work presented in Paper VI, a Scheimpflug configuration was used, but instead of only utilizing two separate wavelength lasers, a tunable narrow-band CW laser was used. Similar to TDLAS and GASMAS (Chapter 3) measurements, the laser was wavelength tuned by changing the injection current. However, due to low detected signal and read-out noise from the camera, the wavelength was not continuously tuned but instead the wavelength was changed stepwise.

5.2 Experimental setup and CO$_2$ measurements

The laser used in the work presented in Paper VI was a tunable, narrow-linewidth, fiber source [70], containing a seed laser tunable in wavelength between 1571.6 and 1573.0 nm. This wavelength interval overlaps with the absorption band (30012 ⟵ 00001) of CO$_2$. The power of the seed laser, 20 mW, was amplified to an output power of around 1.3 W after the fiber amplifier stage, which used a multimode diode laser as a pump laser. Both the seed and pump lasers were temperature and current controlled, but wavelength tuning was solely done by adjusting the current to the seed laser. After each full wavelength scan, which covered three absorption lines of CO$_2$ (R14, R16 and R18), a background signal was measured. This was performed by setting the injection current on both the seed and pump laser to 0 mA (Fig. 5.2a).
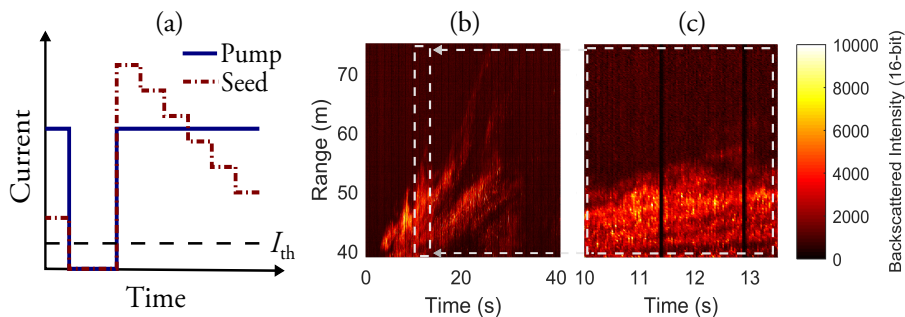
Figure 5.2: Schematic drawing (a) on how the fiber laser system was modulated. When measuring the background both the pump (blue line) and seed (red dotted line) was turned off, i.e. current was set to below the threshold current for lasing (I_{th}). In (b) an example of the backscattered signal when emission from a vehicle passed through the laser beam. In (c) the background measurement, when the laser system is turned off, is visible as dark bands in the image.

The backscattered light was collected by a Newtonian telescope, and an InGaAs line camera was used for signal detection. The data was read out from the camera as matrices with the two dimensions representing range and time (Fig. 5.2b). A long-pass filter was placed in front of the camera. However, it was not sufficient to completely block the background light due to the sun, and therefore daylight measurements were not possible since the detector would drown in background light.

The range scale as shown in Fig. 5.2, was obtained through mapping pixel

number to range through a non-linear function. This procedure requires that the corresponding range for at least one pixel is known. Such information was obtained by performing a calibration measurement where the laser beam was terminated at a known distance. The angular dependence of the range function means that the laser beam has higher range resolution the closer it is to the detector. This is why the first 1000 pixels only cover approximately 80 m, while further away each pixel corresponds to an increasing volume (Fig. 5.3).
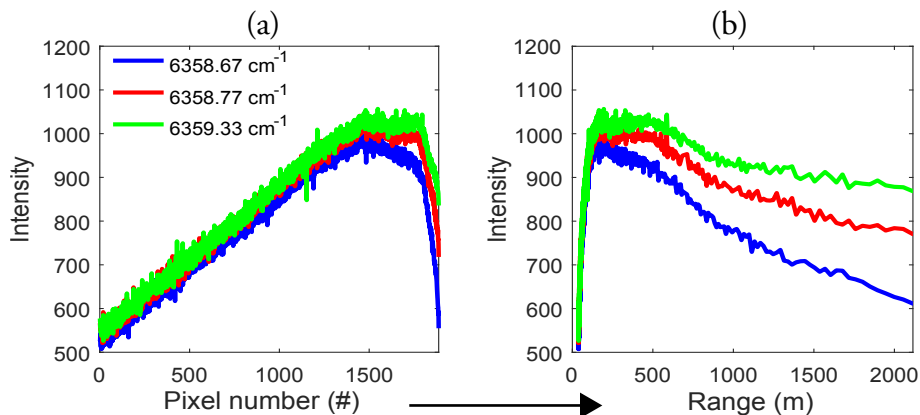

Figure 5.3: (a) Measured backscattered signal at three different wavelengths, on the absorption peak (blue), slope (red) and off resonance (green), as a function of pixel number on the detector. Mapping from pixel number to range (b) is a non-linear function with higher resolution in the near-field.

When evaluating the Scheimpflug Lidar signals, DIAL curves were generated by identifying the off-resonance signals and using the mean as $P(\lambda_{\text{off}}, r)$ in Eq. (5.1). Although the absorption cross section at 1572.6 nm is relatively weak and the concentration of CO_2 in the atmosphere is low, it is clearly observable in Fig. 5.3b due to the long absorption path length. To evaluate the CO_2 concentration, the number density N_{CO_2} was obtained by dividing $P(\lambda_{\text{off}}, r)$ with the signals $P(\lambda_i, r)$, taking the logarithm and for a chosen bin size, Δr, finding the slope, i.e., taking the derivative. Instead of just calculating N_{CO_2} for the peak resonance value, the value of the derivative for all λ_i are fitted to Lorentzian lineshapes (Eq. (2.10)), utilizing that the laser was tuned over three absorption lines. From the lineshape fitting and absorption cross section, $\sigma_{\lambda_{\text{on}}}$, from HITRAN [71], N_{CO_2} was calculated and a concentration in ppm was obtained by using the ideal gas law with a temperature measured by a thermometer outside the laboratory window.

The results presented in Paper VI show that it is possible to measure a reasonable value of CO_2 using Scheimpflug Lidar, with a precision improved by sacrificing range resolution or increased averaging of the signal, thus loosing temporal resolution (Fig. 5.4). However, there seems to be a bias towards lower evaluated concentrations for Δr that are further away from the detector. What is thought to be the main reason originates from the non-linear relationship between pixels and range. An error in the range estimate will lead to an error, or offset, in determining the derivative. Since the range is non-linear, an offset will appear, and that is why the CO_2 concentration is observed to decrease for larger distances (Fig. 5.5).
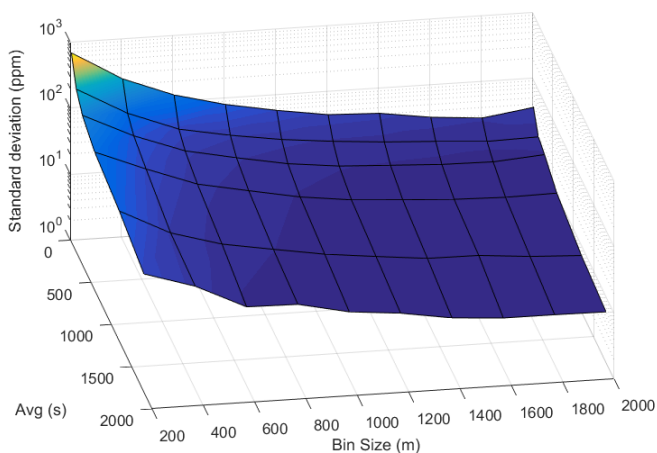

Figure 5.4: The standard deviation for evaluated CO_2 concentration (ppm) at a mean distance of 1000 m from the detector as a function of bin size and averaging time of the collected signals.
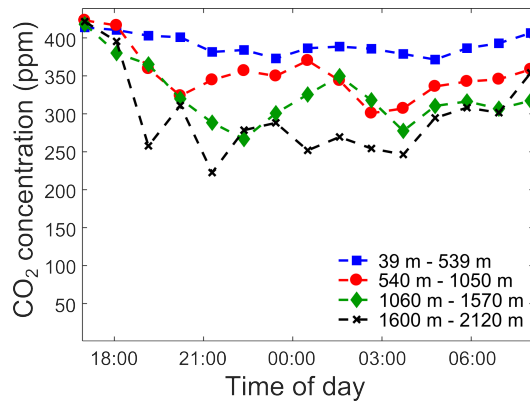
Figure 5.5: CO_2 concentrations evaluated from 17:00 on the 7th of January 2018 until 08:00 on the 8th of January 2018. Here CO_2 concentration is evaluated in range intervals of 500 m.

Chapter 6

Raman spectroscopy

6.1   Raman spectroscopy

The phenomenon that electromagnetic radiation is inelastically scattered by molecules is known as Raman scattering, named after the scientist who was the first to observe the already predicted process of inelastic scattering. In the interaction between electromagnetic radiation and molecules, the molecules may in the scattered process either absorb or contribute some of its internal energy to the outgoing photon. The frequency of the scattered light is said to be Raman shifted and the shift will correspond to the change of energy of the molecules. Raman shifted light with a decrease of energy, or detected at longer wavelengths, is commonly known as Stokes lines and light shifted to shorter wavelengths is known as anti-Stokes lines. The Raman scattered light can be used to investigate molecular structure, i.e. vibrational and rotational, since the energy shift corresponds to the transition energy between vibrational and rotational states in the molecule.

Not all vibrational modes of a molecule produce Raman scattering. In order for a molecule to be Raman active there needs to be a large enough change of polarizability in the molecule during vibrational motion. Also, some molecules can be Raman active but IR inactive, like homonuclear molecules, e.g., N_2 and O_2. In Fig. 6.1, measured Raman spectra of N_2 are presented to demonstrate Raman scattering. Due to the small energy spacing, pure rotational Raman spectra (Fig. 6.1a) are observed close to the Rayleigh line, while the vibrational transition in N_2 corresponds to larger Raman shifts, i.e., located at 2330 cm^{-1} (Fig. 6.1b and c).
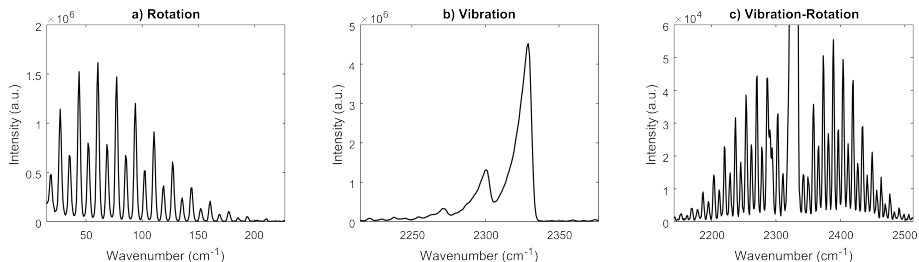
Figure 6.1: (a) Rotational Raman spectrum of N_2, (b) vibrational Raman spectrum at elevated temperature and (c) highly resolved vibrational Raman spectrum of N_2 (at room temperature) with clearly visible rotational fine structure.

6.2   Experimental setup

In the studies, either a pulsed frequency doubled Nd:YAG or Nd:YLF laser was used as light source, with emission wavelengths at 529 and 527 nm, respectively. The laser pulse duration was about 10 ns for both lasers and a repetition frequency of 5 kHz and 1 kHz, respectively. Average output power was about 40 and 25 W, respectively. In order to enhance the Raman signal, the laser light was aligned into two concave mirrors, working as a multipass cell, with around 30 passes, and the light was collected at a 90° degree angle relative to the direction of the laser light. In addition, a mirror was placed 180° from the collection lens in order to enhance the collected signal by a factor of two. The collected light was, after passing through a long-pass filter, spectrally resolved using a spectrometer with an intensified CCD camera. The light passing through the collection lens was focused onto the slit of the spectrometer and imaged along the laser beam, and the probe volume was over the width of light bundle created by the multipass arrangement.

6.3   Periodic shadowing

The spectrometer slit was encoded with a periodic pattern. By encoding the light that was passing through the slit with a spatial frequency, the slit imaged on to the camera can be distinguished from background signals originating from stray light inside the spectrometer. The filtering was performed in the post-processing of the signal using digital lock-in techniques. In many ways it is similar to how the harmonic signals in WMS (Sect. 3.2) are obtained, although generation of the signals are different in PS and WMS.

A visualization of the data, or image, at different steps of the filtering process

is shown in Fig. 6.2, and in this section the filtering process will be explained. The spectrally resolved image has a spatial modulation in the x direction (Fig. 6.2a). Let the detected signal be a function, $S(x, \tilde{v})$, of the wavenumber, $\tilde{v}$, representing the position of the spectrally resolved lines. Since the spatial modulation is along the x direction, all operations in the filtering will also be performed along this direction. Therefore, the function is reduced to be $S_{\tilde{v}}(x) = S(x)$. The spatial modulation will have a center frequency, f_{PS}, depending on the physical modulation of the periodic shadowing. In this study two different ways of creating periodic shadowing were employed, i.e., a glass plate Ronchi grating and an optical fiber bundle. These will be discussed in following sections.

Ideally the signal, $S(x)$, with a spatial modulation along the x direction can be described as:

$$S(x) = A(x) \sin\left(2\pi f_{PS}x\right) + S_{BG}(x), \tag{6.1}$$

where $A(x)$ is the amplitude of the modulation and $S_{BG}(x)$ is a background signal. The amplitude $A(x)$ contains the information of interest as it is the light that has passed through the slit and then been imaged onto the camera, and S_{BG} contains signals originating from stray light in the spectrometer and detector noise. The frequency, f_{PS}, can be retrieved by taking the Fourier transform of the image $S(x, v)$ in the x direction, as is illustrated in Fig. 6.2b. Multiplying $S(x)$ with a reference signal, $S_{ref}(x)$, with a frequency equal to the frequency of the periodic shadowing, $f_{ref} = f_{PS}$ and with an arbitrary phase φ, creates a new signal, $S^*(x) = S(x) \cdot S_{ref}(x)$:

$$S^*(x) = \left(A(x) \sin\left(2\pi f_{PS}x\right) + S_{BG}(x)\right) \sin(2\pi f_{PS}x + \varphi) \tag{6.2}$$

The signal $S^*(x)$ is shown in Fig. 6.2c, where a new periodic pattern is visible, i.e., at frequency f_{ref}. By looking in the Fourier transform (Fig. 6.2d), the signal at f_{PS} has now been shifted to zero frequency, as can be shown by expanding the equation above:

$$S^*(x) = \frac{A(x)}{2} \cos\varphi - \frac{A(x)}{2} \cos(4\pi f_{PS}x + \varphi) + S_{BG}(x) \sin(2\pi f_{PS}x + \varphi). \tag{6.3}$$

A low-pass filter applied to Eq. 6.3 filters out everything except the component $\frac{A(x)}{2} \cos\varphi$, i.e., the zero-frequency Fourier component in Fig. 6.2d. The zero frequency component is maximized when the phase difference, φ, between $S(x)$ and $S_{ref}(x)$ is zero. Instead of manually finding the phase, one can multiply $S(x)$

with a second reference signal that is phase shifted $\varphi + \frac{\pi}{2}$. After multiplication
with the two reference signals one obtains $S_\varphi^*(x)$ and $S_{\varphi+\frac{\pi}{2}}^*(x)$. The amplitude
$A(x)$ can then be obtained from:

$$2\sqrt{S_\varphi^*(x)^2 + S_{\varphi+\frac{\pi}{2}}^*(x)^2} = 2\sqrt{(\frac{A(x)}{2}\cos\varphi)^2 + (\frac{A(x)}{2}\cos(\varphi+\frac{\pi}{2}))^2}$$
$$= A(x)\sqrt{\cos^2\varphi + \cos^2(\varphi+\frac{\pi}{2})}$$
$$= A(x). \tag{6.4}$$

Performing the above described operations for each value of ν in $S(x,\nu)$ results in
an image where $A(x)$ is obtained. Integrating the signal along x gives the spectrum
as show in Fig. 6.2f, where the original signal is compared to the filtered one.

It may be worth mentioning that the signal $S_{BG}(x)$ in Eq. 6.2, is assumed to
be slowly varying in x. If $S_{BG}(x)$ contains a frequency component close to f_{PS},
that one will also be shifted to zero frequency and will not be filtered out by the
low-pass filter.

In the description above on how to perform the filtering in periodic shadow-
ing, the signal was described as being a pure sinusoidal with some varying am-
plitude and background. The periodic shadowing was both tested with a Ronchi
grating and an optical fiber bundle, which does not give a pure sinusoidal pattern.
However, as long as it carries a main frequency component the steps explained in
this section will hold and the filtering can be successfully carried out properly.
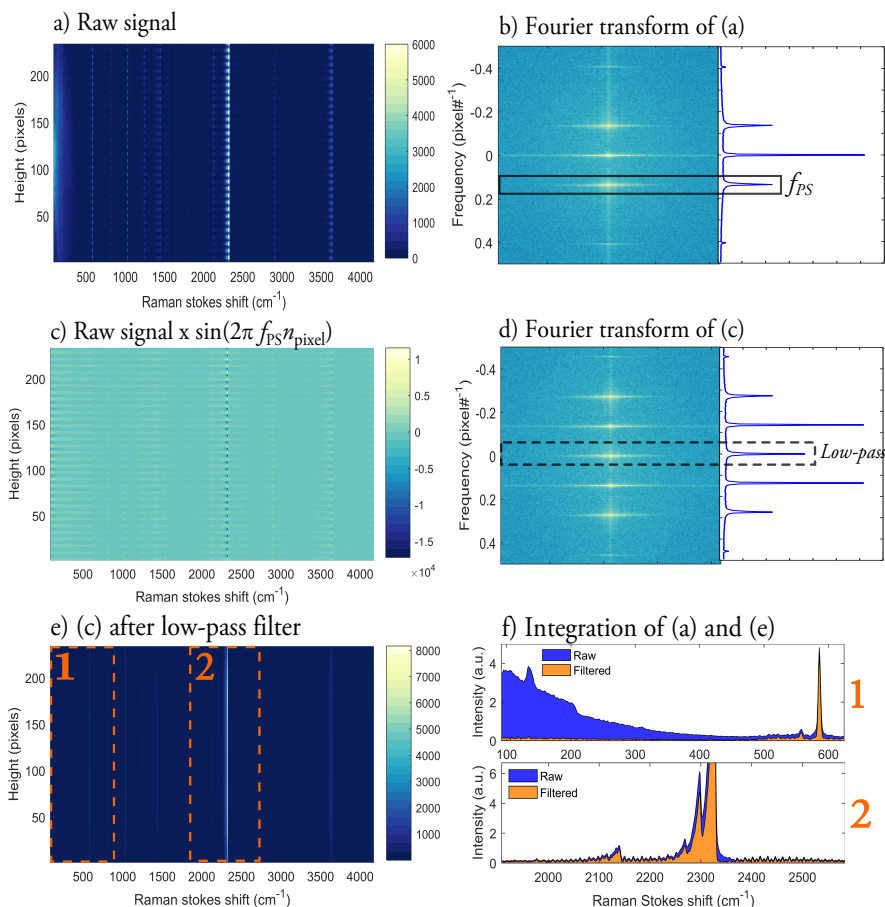
Figure 6.2: The raw signal (a) with periodic shadowing (PS). By taking the Fourier transform (b) it is possible to identify the frequency, f_{PS}, created by PS. Multiplying the raw signal with a sinusoidal with a frequency f_{PS} shifts the information at f_{PS} to zero frequency (c). Applying a low-pass filter only keeps the information at f_{PS} and suppresses stray light in the spectrum (f).

6.3.1 Periodic shadowing with Ronchi grating

The periodic shadowing was used for Raman measurements in different flames. In Fig. 6.3a, evaluated concentration for a methane/hydrogen flame, with a fuel-air equivalence ratio, ϕ, of 0.8, is presented as a function of height above burner (HAB). A porous plug, McKenna burner was used, with a co-flow of N_2 and a

stabilizer (Fig. 6.3b). The flame was lifted which is observed as an offset of the HAB. Measurements were also performed for $\phi = 1, 1.1$, and on ethane-air flames with different ϕ values. The aim of performing concentration and temperature measurements in what can be described as "simple" flames, i.e. burning under laminar conditions, is to provide data for validation of chemistry models.

Concentration is evaluated by integrating the identified Raman peaks. Fractional concentration is obtained by normalization against the spectra and weighting the integrated Raman lines with the Raman cross sections.
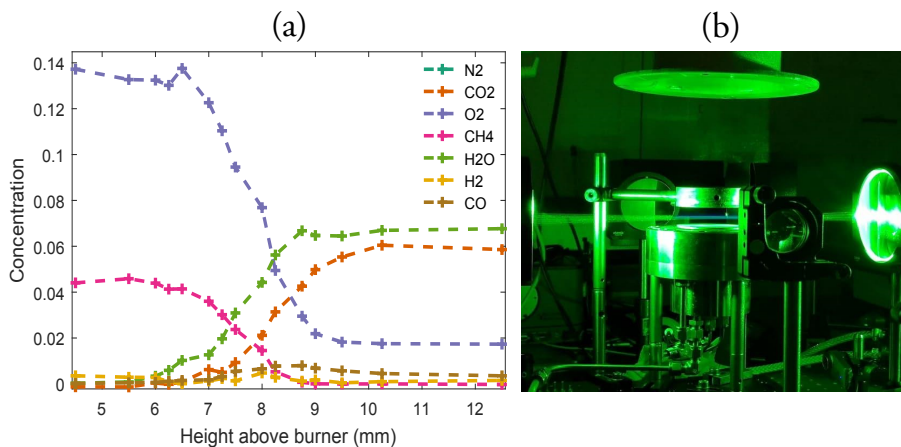
Figure 6.3: (a) Raman measurement in a methane/hydrogen flame with $\phi = 0.8$. (b) A picture of this flame and the McKenna burner with a stabilizer mounted above the burner.

6.3.2 Periodic shadowing with optical fiber

In the previously mentioned flame measurements, a Ronchi grating was used to create the period shadowing. In a second approach, we instead used a special arrangement with an optical fiber bundle to achieve the periodic shadowing. At the output of the bundle, the individual fibers were distributed over the slit of the spectrometer, and periodic shadowing was created by having every other fiber being dark. In Fig. 6.4, the stray is shown to be heavily suppressed close to the laser line when flowing the probe volume with either pure N_2 or O_2. In addition, the periodic shadowing suppress out much of the background noise from the detector, which is why no backgrounds signals were measured and subtracted in the previously mentioned measurements. However, for Raman measurements, as discussed in Sect. 6.3, this only works when Raman scattering is the only contribution to

the signal coming from the probe volume. For example, measurements in fuel rich flames or sources generating strong fluorescence will also give rise to a periodic pattern on the camera, which has to be accounted for in other ways. This can be done through fitting procedures or measuring a background signal.

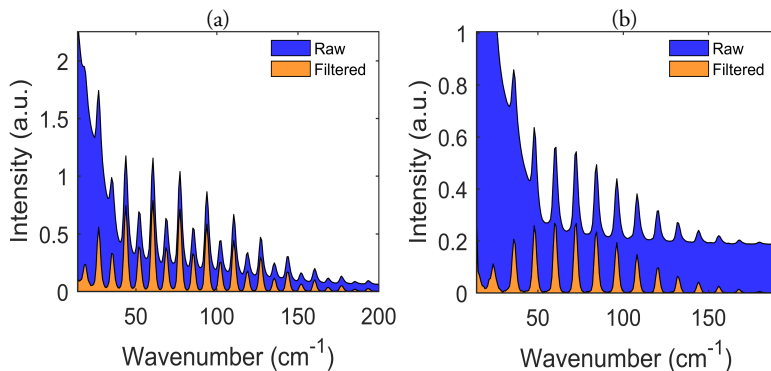**Figure 6.4:** Rotational Raman spectra of (a) N_2 and (b) O_2. The blue area represents the recorded spectrum and the orange area represents the spectrum after filtering with periodic shadowing.

Chapter 7

Conclusion and Outlook

Medical applications

The 3D-printed phantoms presented in Papers II and III, were created for initial test of the GASMAS systems and the intention was for the phantom to be a tool for planning upcoming clinical trials in the project. Previous investigations in the project were GASMAS studies on wild boar [72] and infant lungs [11]. In the studies on the first version of the phantom, reported in Paper II, it was found that the absorption magnitude was significantly higher than what would be expected in a clinical scenario. The improved approach presented in Paper III, with smoother printing and a more realistic lung model, showed more promising results regarding oxygen concentrations, and it was also, to the knowledge of the author, the first time an oxygen concentration was estimated using an absorption path length determined from the H_2O absorption at 820 nm. Previously, H_2O absorption measurements have in the context of the GASMAS technique been done using the absorption band at 935 nm. The change to 820 nm was motivated by the scattering properties of the light being more similar to those at 760 nm than what light with a wavelength of 935 nm would be. This choice comes with a trade-off, which is that the absorption cross section at 820 nm is one order of magnitude lower than at 935 nm (Fig. 4.2b). Therefore, water vapor absorption at this weaker band should only be considered when evaluating O_2 concentrations from the absorption band around 760 nm.

The development of tissue phantoms using 3D-printing technology has been of great interest during recent years, especially for CT and MRI studies. This trend will probably continue [73]. An improved model based on the phantoms presented in Papers II and III is currently being developed [74], where some of

the drawbacks with using a liquid phantom are eliminated by printing solid organs with transparent silicone rubber as the bulk material. Another interesting direction of 3D-printing is so-called bioprinting [75], with a potential to create transplantation organs.

In the work presented in Paper III, the diffuse optical fiber was also used for the first time to experimentally investigate the possibility of illuminating from the interior of the body, which was initially discussed in [76]. It was observed that improvements in both absorption and transmitted intensity were achieved compared to the earlier method of placing the light source on the skin. Therefore the internal light approach was decided to be part of the measurement procedure in the pre-clinical study on anesthetized piglets, presented in Paper IV. One of the main conclusions from the study was that internal illumination, whenever possible, is to be preferred over light administration through the skin. For most of the cases, no consistent detectable signal was obtained from the piglets when using the dermal measurement protocol, and in the best cases only O_2 absorption was obtained for a full measurement series. The fact that it was difficult to obtain absorption signal from H_2O can be explained by the lower output power of the laser at 820 nm, and that the cross section is comparable to that of O_2 at 764 nm, but with a lower concentration for H_2O. Therefore, from the pre-clinical studies, it can be concluded that internal illumination should be of interest to investigate further in a clinical study, where the diffuse fiber would be implemented through the food pipe (esophagus) using a nasogastric tube. Furthermore, it is possible that one could optimize the diffuse fiber by allowing the diffused light to be emitted within a narrower solid angle, thereby allowing more light to go towards the lungs, instead of being emitted at 360 degrees around the fiber.

During the pre-clinical studies, the lung complications atelectasis and pneumothorax were also studied. Unfortunately, due to system limitations, oxygen and water vapor absorption could not be measured simultaneously. However, this should be possible by either distinguishing the signals by scanning over the absorption lines at different times, or by using WMS and modulate the signals at different frequencies [77]. Nevertheless, both O_2 and H_2O were measured to evaluate the oxygen concentration and a trend could be observed as the composition changed. The spread in the data was quite large and the evaluated O_2 concentrations differed between the different piglets, much due to low light transmission and weak absorption signals. In order to obtain better results, higher output power would be preferable since the diode laser at 820 nm only provided around 8 mW. Another limitation that is a common problem in both TDLAS and GASMAS is the

interference fringes that arise. There are various methods for reducing these, e.g., the optics can be angled relative to the laser light propagation direction, or optics can be vibrated to dither the fringes and in that way "average them out". Another very attractive method would be to apply balanced detection [78]. In this method, a reference detector is used and a small portion of the laser light is collected before it is sent into the probe volume, which allows subtracting most effects of the interference fringes that arise in the optics. Balanced detection would also eliminate the need to use nitrogen for flushing the optics box to remove offset signals, since the offset signal would be present on the reference signal and thus be subtracted.

In general, for the GASMAS technology, there are interesting areas of research that should be explored. One that could be of particular interest for medical applications is the possibility of applying multiple detectors and perform diffuse optical tomography [79], with GASMAS. Even without performing tomography, applying more detectors, e.g., one covering each of the different lobes in the lung (further discussed in [76]), could enable faster diagnosis, and should therefore be further explored in the framework of lung monitoring of preterm infants.

Optical remote sensing

The results presented in Paper IV are the very first where CO_2 has been measured with a narrow-band laser using DIAL together with Scheimpflug Lidar. From the DIAL curves, a concentration of around 400 ppm was obtained, which is a reasonable value compared to theglobal average value. It was observed that the precision was dependent on the bin size and the average integration time, as expected, but that there was also a systematic error in the evaluated CO_2 concentration depending on if the signal was evaluated in the near or far-field. A major contributing factor to this uncertainty may come from constant errors that arise in the nonlinear range calibration. This could be improved by having more calibration points placed further away since the range calibration has much better accuracy for ranges before than after the calibration point.

It could also be of interest to use tunable diode lasers with emission at longer wavelengths. For example, a factor 100 can be gained in absorption cross section using the CO_2 absorption band at 2.1 μm instead of the band at 1.6 μm. However, thermal noise from the background and electronics makes this approach somewhat more challenging since it requires a camera that has to be cooled down. The absorption band of H_2O at 935 nm, which has been commonly used in GASMAS, could also be of interest for atmospheric remote sensing with Scheimpflug Lidar.

Raman spectroscopy

In this thesis work, some initial results are presented where periodic shadowing has been employed for Raman spectroscopy. Although it may be somewhat early to draw definitive conclusions, the method of suppressing stray light appears to most effective when studying rotational Raman lines, since stray light is more prominent close to the laser line. Further evaluation of the data is needed to determine the performance of periodic shadowing when evaluating temperatures and concentrations.

Bibliography

[1] W. Haynes, *CRC Handbook of Chemistry and Physics*, ch. 14: Geophysics, Astronomy and Acoustics, pp. 14–19. CRC Press, 2016.

[2] H. Kawahara, T. Matsuo, M. Takami, Y. Fujii, T. Kotani, N. Murakami, M. Tamura, and O. Guyon, "Can ground-based telescopes detect the oxygen 1.27 μm absorption feature as a biomarker in exoplanets?," *The Astrophysical Journal*, vol. 758, no. 1, p. 13, 2012.

[3] S. Kulasooriya, "Cyanobacteria: Pioneers of Planet Earth," *Ceylon Journal of Science (Bio. Sci.)*, vol. 40, no. 2, pp. 71–88, 2011.

[4] S. Solomon, G.-K. Plattner, R. Knutti, and P. Friedlingstein, "Irreversible climate change due to carbon dioxide emissions," *Proceedings of the National Academy of Sciences*, vol. 106, no. 6, pp. 1704–1709, 2009.

[5] J. Blunden, D. S. Arndt, and G. Hartfield, "State of the Climate in 2017," *Bull. Amer. Meteor. Soc.*, vol. 99, no. 8, 2018.

[6] S. R. Morrison, "Semiconductor gas sensors," *Sensors and Actuators*, vol. 2, pp. 329–341, 1981.

[7] M. Jones and T. Nevell, "The detection of hydrogen using catalytic flammable gas sensors," *Sensors and Actuators*, vol. 16, no. 3, pp. 215–224, 1989.

[8] S. Svanberg, *Atomic and Molecular Spectroscopy: Basic Aspects and Practical Applications*, vol. 6. Springer Science & Business Media, 2012.

[9] J. E. Lawn, S. Cousens, and J. Zupan, "4 million neonatal deaths: When? Where? Why?," *The Lancet*, vol. 365, no. 9462, pp. 891 – 900, 2005.

[10] E. J. Hall, "Lessons we have learned from our children: cancer risks from diagnostic radiology," *Pediatric Radiology*, vol. 32, no. 10, pp. 700–706, 2002.

[11] E. Krite Svanberg, P. Lundin, M. Larsson, J. Åkeson, K. Svanberg, S. Svanberg, S. Andersson-Engels, and V. Fellman, "Diode laser spectroscopy for noninvasive monitoring of oxygen in the lungs of newborn infants," *Pediatric Research*, vol. 79, no. 4, p. 621, 2016.

[12] P. Lundin, E. Krite Svanberg, L. Cocola, M. Lewander Xu, G. Somesfalean, S. Andersson-Engels, J. Jahr, V. Fellman, K. Svanberg, and S. Svanberg, "Noninvasive monitoring of gas in the lungs and intestines of newborn infants using diode lasers: feasibility study," *Journal of Biomedical Optics*, vol. 18, no. 12, p. 127005, 2013.

[13] K. E. Trenberth, J. T. Fasullo, and J. Kiehl, "Earth's global energy budget," *Bulletin of the American Meteorological Society*, vol. 90, no. 3, pp. 311–324, 2009.

[14] M. Brydegaard, A. Gebru, and S. Svanberg, "Super resolution laser radar with blinking atmospheric particles - Application to interacting flying insects," *Progress In Electromagnetics Research*, vol. 147, pp. 141–151, 2014.

[15] M. Brydegaard, E. Malmqvist, S. Jansson, J. Larsson, S. Török, and G. Zhao, "The Scheimpflug lidar method," in *Lidar Remote Sensing for Environmental Monitoring 2017*, vol. 10406, p. 104060I, International Society for Optics and Photonics, 2017.

[16] E. Malmqvist, M. Brydegaard, M. Aldén, and J. Bood, "Scheimpflug lidar for combustion diagnostics," *Optics Express*, vol. 26, no. 12, pp. 14842–14858, 2018.

[17] A. C. Eckbreth, P. A. Bonczyk, and J. F. Verdieck, "Combustion diagnostics by laser Raman and fluorescence techniques," *Progress in Energy and Combustion Science*, vol. 5, no. 4, pp. 253–322, 1979.

[18] E. Kristensson, J. Bood, M. Alden, E. Nordström, J. Zhu, S. Huldt, P.-E. Bengtsson, H. Nilsson, E. Berrocal, and A. Ehn, "Stray light suppression in spectroscopy using periodic shadowing," *Optics Express*, vol. 22, no. 7, pp. 7711–7721, 2014.

[19] J. Sakurai and J. Napolitano, *Modern Quantum Mechanics*. Cambridge University Press, 2017.

[20] M. Born and R. Oppenheimer, "On the quantum theory of molecules," in *Quantum Chemistry: Classic Scientific Papers*, pp. 1–24, World Scientific, 2000.

[21] C. Schutte, J. Bertie, P. Bunker, J. Hougen, I. Mills, J. Watson, and B. Winnewisser, "Notations and conventions in molecular spectroscopy: Part 2. Symmetry notation (iupac recommendations 1997)," *Pure and Applied Chemistry*, vol. 69, no. 8, pp. 1641–1650, 1997.

[22] A. Einstein, "Zur Quantentheorie der Strahlung," *Phys. Z.*, vol. 18, pp. 121–128, 1917.

[23] J. H. Lambert, *Photometria Sive de Mensura et Gradibus Luminis, Colorum et Umbrae*. Augsburg, 1760.

[24] A. Beer, "Bestimmung der Absorption des rothen Lichts in farbigen Flüssigkeiten," *Ann. Physik*, vol. 162, pp. 78–88, 1852.

[25] I. Gordon, L. Rothman, C. Hill, R. Kochanov, Y. Tan, P. Bernath, M. Birk, V. Boudon, A. Campargue, K. Chance, B. Drouin, J.-M. Flaud, R. Gamache, J. Hodges, D. Jacquemart, V. Perevalov, A. Perrin, K. Shine, M.-A. Smith, J. Tennyson, G. Toon, H. Tran, V. Tyuterev, A. Barbe, A. Császár, V. Devi, T. Furtenbacher, J. Harrison, J.-M. Hartmann, A. Jolly, T. Johnson, T. Karman, I. Kleiner, A. Kyuberis, J. Loos, O. Lyulin, S. Massie, S. Mikhailenko, N. Moazzen-Ahmadi, H. Müller, O. Naumenko, A. Nikitin, O. Polyansky, M. Rey, M. Rotger, S. Sharpe, K. Sung, E. Starikova, S. Tashkun, J. V. Auwera, G. Wagner, J. Wilzewski, P. Wcisło, S. Yu, and E. Zak, "The HITRAN 2016 molecular spectroscopic database," *Journal of Quantitative Spectroscopy and Radiative Transfer*, vol. 203, pp. 3 – 69, 2017.

[26] W. Demtröder, *Atoms, Molecules and Photons: An Introduction to Atomic-, Molecular- and Quantum Physics*, ch. Emission and Absorption of Electromagnetic Radiation by Atoms, pp. 247–288. Berlin, Heidelberg: Springer Berlin Heidelberg, 2010.

[27] G. W Collins, *The Fundamentals of Stellar Astrophysics*, ch. Shape of Spectral Lines, pp. 348–397. New York: W. H. Freeman and Co.., 1989.

[28] J. H. van Vleck and V. F. Weisskopf, "On the shape of collision-broadened lines," *Reviews of Modern Physics*, vol. 17, no. 2-3, p. 227, 1945.

[29] C. J. Tsao and B. Curnutte, "Line-widths of pressure-broadened spectral lines," *Journal of Quantitative Spectroscopy and Radiative Transfer*, vol. 2, no. 1, pp. 41–91, 1962.

[30] A. Jabloński, "General theory of pressure broadening of spectral lines," *Physical Review*, vol. 68, no. 3-4, p. 78, 1945.

[31] L. Brown and C. Plymate, "Experimental line parameters of the oxygen a band at 760 nm," *Journal of Molecular Spectroscopy*, vol. 199, no. 2, pp. 166–179, 2000.

[32] R. R. Gamache and J. Lamouroux, "Predicting accurate line shape parameters for CO_2 transitions," *Journal of Quantitative Spectroscopy and Radiative Transfer*, vol. 130, pp. 158–171, 2013.

[33] S. D. Gasster, C. H. Townes, D. Goorvitch, and F. P. Valero, "Foreign-gas collision broadening of the far-infrared spectrum of water vapor," *JOSA B*, vol. 5, no. 3, pp. 593–601, 1988.

[34] R. N. Hall, G. E. Fenner, J. D. Kingsley, T. J. Soltys, and R. O. Carlson, "Coherent light emission from GaAs junctions," *Phys. Rev. Lett.*, vol. 9, pp. 366–368, Nov 1962.

[35] E. Hinkley, "High-resolution infrared spectroscopy with a tunable diode laser," *Applied Physics Letters*, vol. 16, no. 9, pp. 351–354, 1970.

[36] M. Lackner, "Tunable diode laser absorption spectroscopy (TDLAS) in the process industries - a review," *Reviews in Chemical Engineering*, vol. 23, no. 2, pp. 65–147, 2007.

[37] P. Hofmann, *Solid State Physics: An Introduction*, ch. on Semiconductors, pp. 113–133. John Wiley & Sons, 2015.

[38] S. Schilt, L. Thevenaz, and P. Robert, "Wavelength modulation spectroscopy: combined frequency and intensity laser modulation," *Applied Optics*, vol. 42, no. 33, pp. 6728–6738, 2003.

[39] E. A. Whittaker, M. Gehrtz, and G. C. Bjorklund, "Residual amplitude modulation in laser electro-optic phase modulation," *J. Opt. Soc. Am. B*, vol. 2, no. 8, pp. 1320–1326, 1985.

[40] M. Sjöholm, G. Somesfalean, J. Alnis, S. Andersson-Engels, and S. Svanberg, "Analysis of gas dispersed in scattering media," *Optics Letters*, vol. 26, no. 1, pp. 16–18, 2001.

[41] S. Svanberg, "Gas in scattering media absorption spectroscopy - from basic studies to biomedical applications," *Laser & Photonics Reviews*, vol. 7, no. 5, pp. 779–796, 2013.

[42] EUROSTARS, "Development of neonate bedside lung monitoring sensor based on diode laser spectroscopy," Oct 2015.

[43] L. E. Simmons, C. E. Rubens, G. L. Darmstadt, and M. G. Gravett, "Preventing preterm birth and neonatal mortality: Exploring the epidemiology, causes, and interventions," *Seminars in Perinatology*, vol. 34, no. 6, pp. 408 – 415, 2010.

[44] D. Shier, J. Butler, and R. Lewis, *Hole's Essentials of Human Anatomy & Physiology*, ch. 19. Respiratory System, pp. 753–790. McGraw-Hill Education New York, 2015.

[45] W. A. Engle, K. M. Tomashek, and C. Wallman, ""late-preterm" infants: a population at risk," *Pediatrics*, vol. 120, no. 6, pp. 1390–1401, 2007.

[46] A. H. Jobe and E. Bancalari, "Bronchopulmonary dysplasia," *American Journal of Respiratory and Critical Care Medicine*, vol. 163, no. 7, pp. 1723–1729, 2001.

[47] E. Baraldi and M. Filippone, "Chronic lung disease after premature birth," *New England Journal of Medicine*, vol. 357, no. 19, pp. 1946–1955, 2007.

[48] R. A. Polin, W. A. Carlo, C. on Fetus, A. A. o. P. Newborn, *et al.*, "Surfactant replacement therapy for preterm and term neonates with respiratory distress," *Pediatrics*, vol. 133, no. 1, pp. 156–163, 2014.

[49] S. L. Jacques, "Optical properties of biological tissues: a review," *Physics in Medicine and Biology*, vol. 58, pp. R37–R61, may 2013.

[50] L. Dean, *Blood groups and red cell antigens.* National Center for Biotechnology Information, 2005.

[51] L. Roberts, "The normal ranges, with statistical analysis for seventeen blood constituents," *Clinica Chimica Acta*, vol. 16, no. 1, pp. 69–78, 1967.

[52] K. K. Tremper, "Pulse oximetry," *Chest*, vol. 95, no. 4, pp. 713–715, 1989.

[53] G. J. McRae, "A simple procedure for calculating atmospheric water vapor concentration," *Journal of the Air Pollution Control Association*, vol. 30, no. 4, pp. 394–394, 1980.

[54] C. Hazelaar, M. Eijnatten, M. Dahele, J. Wolff, T. Forouzanfar, B. Slotman, and W. F. Verbakel, "Using 3D printing techniques to create an anthropomorphic thorax phantom for medical imaging purposes," *Medical Physics*, vol. 45, no. 1, pp. 92–100, 2018.

[55] Y. He, Y. Liu, B. A. Dyer, J. M. Boone, S. Liu, T. Chen, F. Zheng, Y. Zhu, Y. Sun, Y. Rong, and J. Qiu, "3d-printed breast phantom for multi-purpose and multi-modality imaging," *Quantitative Imaging in Medicine and Surgery*, vol. 9, no. 1, p. 63, 2019.

[56] I. Hernandez-Giron, J. M. den Harder, G. J. Streekstra, J. Geleijns, and W. J. Veldkamp, "Development of a 3D printed anthropomorphic lung phantom for image quality assessment in CT," *Physica Medica*, vol. 57, pp. 47–57, 2019.

[57] S. Wood, N. Krishnamurthy, T. Santini, S. Raval, N. Farhat, J. A. Holmes, and T. S. Ibrahim, "Design and fabrication of a realistic anthropomorphic heterogeneous head phantom for MR purposes," *PloS One*, vol. 12, no. 8, p. e0183168, 2017.

[58] K. Tappa and U. Jammalamadaka, "Novel biomaterials used in medical 3D printing techniques," *Journal of Functional Biomaterials*, vol. 9, no. 1, p. 17, 2018.

[59] J. Maier, M. Weiherer, M. Huber, and C. Palm, "Imitating human soft tissue on basis of a dual-material 3D print using a support-filled metamaterial to provide bimanual haptic for a hand surgery training system," *Quantitative Imaging in Medicine and Surgery*, vol. 9, no. 1, p. 30, 2019.

[60] H. Dehghani, M. E. Eames, P. K. Yalavarthy, S. C. Davis, S. Srinivasan, C. M. Carpenter, B. W. Pogue, and K. D. Paulsen, "Near infrared optical tomography using NIRFAST: Algorithm for numerical model and image reconstruction," *Communications in Numerical Methods in Engineering*, vol. 25, no. 6, pp. 711–732, 2009.

[61] M. Jermyn, H. R. Ghadyani, M. A. Mastanduno, W. D. Turner, S. C. Davis, H. Dehghani, and B. W. Pogue, "Fast segmentation and high-quality three-dimensional volume mesh creation from medical images for diffuse optical tomography," *Journal of Biomedical Optics*, vol. 18, no. 8, p. 086007, 2013.

[62] P. Liao, J. Larsson, E. Krite Svanberg, P. Lundin, J. Swartling, M. Lewander Xu, J. Bood, and S. Andersson-Engels, "Computer simulation analysis of source-detector position for percutaneously measured O_2-gas signal in a three-dimensional preterm infant lung," *Journal of Biophotonics*, vol. 11, no. 11, p. e201800023, 2018.

[63] D. Khoptyar, A. A. Subash, S. Johansson, M. Saleem, A. Sparén, J. Johansson, and S. Andersson-Engels, "Broadband photon time-of-flight spectroscopy of pharmaceuticals and highly scattering plastics in the vis and close nir spectral ranges," *Optics Express*, vol. 21, no. 18, pp. 20941–20953, 2013.

[64] L. Mei, S. Svanberg, and G. Somesfalean, "Combined optical porosimetry and gas absorption spectroscopy in gas-filled porous media using diode-laser-based frequency domain photon migration," *Optics Express*, vol. 20, no. 15, pp. 16942–16954, 2012.

[65] J. Guillen, "FELASA guidelines and recommendations," *Journal of the American Association for Laboratory Animal Science*, vol. 51, no. 3, pp. 311–321, 2012.

[66] I. Ventrillard-Courtillot, T. Gonthiez, C. Clerici, and D. Romanini, "Multispecies breath analysis faster than a single respiratory cycle by optical-feedback cavity-enhanced absorption spectroscopy," *Journal of Biomedical Optics*, vol. 14, no. 6, p. 064026, 2009.

[67] A. Manolis, "The diagnostic potential of breath analysis.," *Clinical Chemistry*, vol. 29, no. 1, pp. 5–15, 1983.

[68] E. Malmqvist, S. Jansson, S. Zhu, W. Li, K. Svanberg, S. Svanberg, J. Rydell, Z. Song, J. Bood, M. Brydegaard, and S. Åkesson, "The bat–bird–bug battle:

Daily flight activity of insects and their predators over a rice field revealed by high-resolution Scheimpflug lidar," *Royal Society Open Science*, vol. 5, no. 4, p. 172303, 2018.

[69] L. Mei and M. Brydegaard, "Atmospheric aerosol monitoring by an elastic Scheimpflug lidar system," *Optics Express*, vol. 23, no. 24, pp. A1613–A1628, 2015.

[70] X. Yang, R. Lindberg, J. Larsson, J. Bood, M. Brydegaard, and F. Laurell, "1.57 μm fiber source for atmospheric CO_2 continuous-wave differential absorption lidar," *Optics Express*, vol. 27, no. 7, pp. 10304–10310, 2019.

[71] L. S. Rothman, D. Jacquemart, A. Barbe, D. C. Benner, M. Birk, L. Brown, M. Carleer, C. Chackerian Jr, K. Chance, L. Coudert, *et al.*, "The hitran 2004 molecular spectroscopic database," *Journal of Quantitative Spectroscopy and Radiative Transfer*, vol. 96, no. 2, pp. 139–204, 2005.

[72] M. Lewander, A. Bruzelius, S. Svanberg, K. Svanberg, and V. Fellman, "Nonintrusive gas monitoring in neonatal lungs using diode laser spectroscopy: feasibility study," *Journal of Biomedical Optics*, vol. 16, no. 12, p. 127002, 2011.

[73] V. Filippou and C. Tsoumpas, "Recent advances on the development of phantoms using 3D printing for imaging with CT, MRI, PET, SPECT, and ultrasound," *Medical Physics*, vol. 45, no. 9, pp. e740–e760, 2018.

[74] S. K. V. Sekar, A. Pacheco, P. Martella, H. Li, P. Lanka, A. Pifferi, and S. Andersson-Engels, "Solid phantom recipe for diffuse optics in biophotonics applications: a step towards anatomically correct 3D tissue phantoms," *Biomedical Optics Express*, vol. 10, no. 4, pp. 2090–2100, 2019.

[75] S. V. Murphy and A. Atala, "3D bioprinting of tissues and organs," *Nature Biotechnology*, vol. 32, no. 8, p. 773, 2014.

[76] E. Krite Svanberg, *Non-invasive optical monitoring of free and bound oxygen in humans*. Department of Clinical Sciences Malmö, Anesthesiology and Intensive Care Medicine, Lund/Malmö, 2016.

[77] M. Lewander, Z. Guan, K. Svanberg, S. Svanberg, and T. Svensson, "Clinical system for non-invasive in situ monitoring of gases in the human paranasal sinuses," *Optics Express*, vol. 17, no. 13, pp. 10849–10863, 2009.

[78] L. Persson, F. Andersson, M. Andersson, and S. Svanberg, "Approach to optical interference fringes reduction in diode laser absorption spectroscopy," *Applied Physics B*, vol. 87, no. 3, pp. 523–530, 2007.

[79] T. Durduran, R. Choe, W. B. Baker, and A. G. Yodh, "Diffuse optics for tissue monitoring and tomography," *Reports on Progress in Physics*, vol. 73, no. 7, p. 076701, 2010.

Acknowledgements

First, I would like to thank my supervisor *Joakim Bood* for all support, help and for everything I have learned. In addition to your knowledge in the field of physics, I have always been inspired by your excellent language skills, your patience and always extremely well-constructed emails.

Looking back you can say that all this started when, a few years before my PhD education, I stumbled upon the course Atomic and Molecular Spectroscopy led by *Sune Svanberg*. The rest is history and now I am grateful for having you as co-supervisor and for being here to help me finish this journey.

Although our cultural and linguistic differences, I think that you, *Marcus Aldén*, have been a great boss of the Division of Combustion Physics. I have appreciated our discussions about physics, how it is to be a PhD student and the discrepancy between people from Skåne and the rest of Sweden. I also have you to thank for being one of the main reasons I chose to finish my studies.

Christian Brackmann, I am very glad that I, here at the end, got the opportunity to study Raman spectroscopy in your "Raman group". It has been a pleasure and it really feels that I have learned a lot in this relatively short time period. *Haisol Kim*, I hope you enjoyed our Raman measurements as much as I did, I don't know if I am most proud of the plasma cage we built or the shelves we put up. I wish you the best in your future studies.

In the medical project, I am pleased to have worked with you *Emilie Krite Svanberg*. You have been very supportive and put time aside for helping me in my scientific work. In the same spirit, I would especially like to extend my gratitude to *Dennis Leander* and *Sara Bergsten*, who I have also worked closely with. I appreciated every "minced meat" Wednesday.

I would further like to acknowledge the people in the clinical group in the medical research, *Vineta Fellman*, *Katarina Svanberg*, *Linda Nilsson*, *Marcus Larsson*, *Gorm Greisen* and *Martin Rasmussen*. You have supported me with your com-

petence and knowledge as I took part of research outside my previous studies. Many people have contributed to this project and I had the pleasure of working with *Peilang Liao*, *Patrik Lundin*, *Johannes Swartling*, *Märta Lewander Xu*, *Stefan Andersson-Engels*, *Anders Långberg*, *Mikael Sebesta*, and *Hanna Sjöström*. I am truly grateful for your input and help.

I would also like to acknowledge *Mikkel Brydegaard*, who made me venture into the area of remote sensing and bad Danish jokes, and *Samuel Jansson* for helping out with Scheimpflug alignment, evening measurements and painting techniques. I am also happy for the collaboration with *Fredrik Laurell*, *Robert Lindberg* and *Xiong Yang* from the laser physics group at KTH.

Elin Malmqvist, I have always appreciated the teaching, courses and risk analyzes we have done together, along with your always positive attitude. I think that, with some practice, you can one day be a great Senior Advisor.

Andreas Ehn, I have enjoyed and will miss the physics discussions we had in your office, and I wish you the best with the plasma diagnostics.

Cecilia Bille and *Minna Ramkull*, I think that the two of you are very important for the warm working climate at the Division of Combustion Physics and the division is very lucky to have you.

Igor Buzuk, thank you for answering all my stupid questions about computers, electronics and software.

My office mate *Arman Subash*, it has now been almost five years since we started sharing office and I have always valued your good spirit, knowledge and your stash of sweets.

The members of group Bood, *Maria Ruchkina*, *Pengji Ding*, *Kajsa Larsson* and *Malin Jonsson*. I would like to thank you for everything you have helped and supported me with, ranging from applying for grants to giving me training advice, nicknames, carrot cake recipes and lending out equipment. I would also like to acknowledge *Dina Hot* for always having an answer or a reference up her sleeve and *Yupan Bao* for keeping me company off-hours at the division and for our gaming sessions.

With this being said I would like to thank everyone that I have met through the division over these five years. It has been a truly unique experience, and I hope that the division will continue to value the open and friendly working environment that encourages people to help and share.

Finally, I would like to thank my friends and family for putting up with me during this time. There have been some good moments but also very tough ones and even though it sometimes feels like I am constantly tired and bad at keeping

contact, you all matter a lot. I also hope when *Mom* and *Dad* reads the summary, that you will finally have some clue of what I have been busy with these last five years.

Funding

Summary of Papers

Paper I:
Development of a compact multipass oxygen sensor used for gas diffusion studies in opaque media

J. Larsson, M. Liang, P. Lundin, J. Bood, S. Svanberg
Applied Optics, vol. 54, 9772-9778 (2015).

In this work, a porous ceramic sample was designed as a compact random-scattering multipass gas cell and by employing the GASMAS technique, gas transport in different wood materials was studied. The ceramic material enhanced the absorption path length approximately 26 times, and the sensor was inserted into the wood material by pre-drilling. Gas transport was studied for different wood materials and for diffusion longitudinal or radial to the annual rings of the tree. It was observed that very little gas diffused in the radial direction and that the diffusion time was fastest for densest wood material and slowest for the the one with the lowest density.

I was the main responsible for designing, i.e., constructing the sensor probe and preparing the wood materials, and planning the experiment. I performed the measurements, analyzed the data, and I was the main responsible for preparing the manuscript.

Paper II:
Development of a 3-dimensional tissue lung phantom of a preterm infant for optical measurements of oxygen-Laser-detector position considerations

J. Larsson, P. Liao, P. Lundin, E. Krite Svanberg, J. Swartling, M. Lewander Xu, J. Bood, S. Andersson-Engels
Journal of Biophotonics, **11**, e201700097 (2018).

In this work, a 3D-printed tissue phantom was developed based on CT images of the thorax of a 1700 g premature infant. The phantom was employed for investigating different light source and detector positions, using the GASMAS technique for both oxygen and water vapor absorption at 760 nm and 935 nm, respectively. It was observed that stronger gas absorption signals were obtained for light source and detector positions covering the lower part of the lung, which was with the consistent with the air volume distribution of the lung.

I assisted in the 3D reconstruction of the phantom and in making the liquid phantoms. I contributed to the planing of the measurements and I took part in all measurements. I analyzed the data and was the main responsible for preparing the manuscript.

Paper III:
Comparison of dermal versus internal light administration in human lungs using the TDLAS-GASMAS technique -Phantom studies

J. Larsson, D. Leander, M. Lewander Xu, V. Fellman, J. Bood, E. Krite Svanberg
Journal of Biophotonics, e201800350 (2019).

An improved version of the 3D-printed phantom from Paper II was developed for investigating the effect of internally delivery of the laser light using a diffuse optical fiber, where the lung model contained an interior structure. In addition, the oxygen concentration was for the first time evaluated using the water vapor absorption at 820 nm with the GASMAS technique.

In this work, I contributed to the planning and construction of the phantom. I assisted

in planning the measurements and I took part in all measurements. I analyzed the data and was the main responsible for preparing the manuscript.

Paper IV:
Changes in pulmonary oxygen content are detectable with laser absorption spectroscopy: – Proof of concept in newborn piglets

E. Krite Svanberg, **J. Larsson**, M. Rasmussen, M. Larsson, D. Leander, S. Bergsten, J. Bood, G. Greisen, V. Fellman
(To be submitted)

In this work, five anesthetized piglets were studied using the GASMAS technique, measuring O_2 and H_2O absorption at the wavelengths 764 nm and 820 nm, respectively. The light was either delivered externally, on the skin, or internally through the esophagus. The detector was placed on the skin. The oxygen concentration was evaluated at different ventilated concentrations and the oxygen content was studied when inducing lung complications (atelectasis and pneumothorax). It was observed that the absorption and light transmission responded differently for atelectasis and pneumothorax. The oxygen concentration could only be evaluted for the internal light illumination due to the poor signal quality of the H_2O absorption for dermal illumination.

I contributed in the planing of the experiment and the measurement protocol. I took part in all measurements, during which I assisted in the technical instrumentation, i.e., the GASMAS system. I analyzed the data and I assisted in preparing and writing the manuscript.

Paper V:
Short-wave infrared atmospheric Scheimpflug lidar

M. Brydegaard, **J. Larsson**, S. Török, E. Malmqvist, G. Zhao, S. Jansson, M. Andersson, S. Svanberg, S. Åkesson, F. Laurell, J. Bood
EPJ Web Conferences, **176**, 01012 (2018).

Atmospheric dual-band Scheimpflug lidar was demonstrated at 980 and 1550 nm.

Measurements were performed during foggy, clear and snowy weather conditions, and aerosol classification was evaluated by performing particle releases in the atmosphere.

I assisted in building the experimental setup and took part in the measurements.

Paper VI:
Atmospheric CO_2 sensing using Scheimpflug lidar based on a 1.57-μm fiber source

J. Larsson, J. Bood, C. Xu, X. Yang, R. Lindberg, F. Laurell, M. Brydegaard
Optics Express, **27**, 17348-17358 (2019).

In this work, Scheimpflug DIAL measurements of CO_2 in the atmosphere was performed. The light source consisted of a CW diode laser that was amplified by an Erbium-doped fiber amplifier, resulting in an output power of about 1.3 W, at an emission wavelength at 1.57 μm, and a linewidth of 3 MHz. The CO_2 concentration was range-resolved over a distance of 2 km, and a CO_2 concentration close to 400 ppm was evaluated.

I assisted in building the experimental setup and setting up the laser source which was provided by the Department of Applied Physics at KTH (Prof. F. Laurell). I performed the measurements, analyzed the data, and contributed to preparing the manuscript.